*J. Fluid Mech.* (2006), *vol.* 546, *pp.* 313–339. © 2005 Cambridge University Press 
doi:10.1017/S0022112005007111 Printed in the United Kingdom

# Stratified turbulence generated by internal gravity waves

By MICHAEL L. WAITE AND PETER BARTELLO

McGill University, 805 rue Sherbrooke ouest, Montréal, QC H3A 2K6, Canada

(Received 7 January 2005 and in revised form 5 July 2005)

We present numerical simulations of randomly forced internal gravity waves in a uniformly stratified Boussinesq fluid, and compare the resulting vertical wavenumber energy spectra with the saturation spectrum $E_z(k_z) = c\,N^2 k_z^{-3}$ ($N$ is the Brunt–Väisälä frequency) observed in the atmosphere and ocean. Overall, we have been unsuccessful at reproducing the observed spectrum in our simulations. Our spectra are shallower than $k_z^{-3}$, although they steepen towards it with increasing stratification as long as wave breaking (in the form of static instability) is resolved. The spectral amplitude increases like $N^{1.1}$ rather than $N^2$. For a single stratification, our spectrum agrees well with the saturation spectrum with $c = 0.1$, but only because it is spuriously steepened by insufficient resolution. We show that overturning occurs when the length scale $l_c = u_{rms}/N$ is larger than the dissipation scale, where $u_{rms}$ is the root mean square velocity. This scale must be at least three times larger than the dissipation scale for the energy spectrum to be independent of Reynolds number in our simulations. When this condition is not satisfied, the computed energy spectrum must be interpreted with caution. Finally, we show that for strong stratifications, the presence of vortical energy can have a dramatic effect on the spectrum of wave energy due to the efficiency of interactions between two waves and a vortical mode. Any explanation of the energy spectrum involving resonant interactions must take into account the effect of vortical motion.

## 1. Introduction

In the presence of stable density stratification (found in the mean atmosphere and ocean), fluids admit both slow quasi-horizontal vortical motion and fast internal gravity waves (e.g. Riley & Lelong 2000). At large geophysical scales where the Earth's rotation is important, vortical (quasi-geostrophic) motion dominates. Internal waves coexist with vortical motion downscale in the atmospheric mesoscale and oceanic submesoscale, where rotational effects are weaker (e.g. Cho, Newell & Barrick 1999; Polzin *et al.* 2003). At sufficiently small scales, waves and vortices destabilize and break down into turbulence. This process dissipates energy and mixes various quantities, and is parameterized in most large-scale atmosphere and ocean models. In a previous paper, we performed a detailed study of the dynamics and breakdown of vortical motion in a stratified non-rotating fluid (Waite & Bartello 2004). Here, we continue this analysis by examining the generation of turbulence by internal waves (for reviews of internal waves, see Müller *et al.* 1986; Staquet & Sommeria 2002).

A key result from the study of atmospheric and oceanic turbulence is that the vertical wavenumber kinetic energy spectrum is approximately universal. The

https://doi.org/10.1017/S0022112005007111 Published online by Cambridge University Press

atmospheric spectrum often resembles

$$E_z(k_z) = c\,N^2\,k_z^{-3}, \tag{1.1}$$

where $N$ is the Brunt–Väisälä frequency (e.g. Smith, Fritts & VanZandt 1987; Tsuda *et al.* 1989; Allen & Vincent 1995). However, deviations from this spectrum have been reported. Nastrom, VanZandt & Warnock (1997) found spectral amplitudes scaling like $N^{0.6}$ rather than $N^2$, and spectral slopes of only $-2.6$ in the troposphere. In addition, a spectrum of the form $k_z^{-5/3}$ is sometimes observed in place of (1.1) at small scales (1–10 m) (Alisse & Sidi 2000).

In the ocean, the observed energy spectrum is represented by the Garrett–Munk (GM) spectrum, which has the form $k_z^{-2}$, down to scales of around 10 m (see Munk 1981, for a review and the current formulation of the spectrum). Munk (1981) argued that the small-scale end of the GM range is set by the onset of instability, implying a spectral transition at $k_z = k_c \equiv N/u_{rms}$, where $u_{rms}$ is the root mean square (r.m.s.) velocity. Downscale of the GM range, the energy spectrum resembles (1.1) (Gargett *et al.* 1981). When the Ozmidov buoyancy scale $l_b = (\epsilon/N^3)^{1/2}$ is sufficiently larger than the dissipation scale $l_d = (\nu^3/\epsilon)^{1/4}$ ($\epsilon$ is the energy dissipation rate and $\nu$ is the kinematic viscosity), a transition at $k_b = 1/l_b$ from (1.1) to the isotropic Kolmogorov spectrum $\epsilon^{2/3}k^{-5/3}$ is observed (Gargett *et al.* 1981; Gargett, Osborn & Nasmyth 1984). The transition from $k^{-3}$ to $k^{-5/3}$ at $k_b$ has been predicted by different theories (Lumley 1964; Holloway 1983).

The spectra observed in the atmosphere and ocean are generally attributed to internal wave processes, but the details are not well-understood. In the atmosphere, the spectrum is thought to result from saturating internal waves. Vertically propagating waves grow with height until they become unstable and break. The limiting spectrum in which all waves are on the threshold of breaking is called the saturation spectrum. The simplest models of this process are the linear saturation theories, which assume linear instability as the breaking mechanism and predict a spectrum of the form (1.1) (Dewan & Good 1986; Smith *et al.* 1987). The linear saturation theories are widely accepted because they appear to explain the observations. However, their theoretical foundations have been seriously undermined, particularly the assumption that waves at different wavenumbers saturate independently (Hines 1991). Breaking is fundamentally not a spectral process; it occurs when all waves superpose to produce a region of instability. At most, the linear saturation theories yield an upper bound on the true saturation spectrum. Hines (1991, 1996) has proposed a theory of nonlinear saturation, in which Doppler shifting of small waves by large ones determines the spectrum. He argues that the transition between the linear and nonlinear (i.e. unsaturated and saturated) parts of the spectrum occurs at $k_z = k_c$, as suggested by Munk (1981) for the oceanic spectrum.

For the ocean, there was substantial debate in the early 1980s about whether the GM spectrum, which satisfies the internal wave dispersion and polarization relations, is composed of weakly or strongly interacting waves, and the issue has not been fully resolved (e.g. McComas & Müller 1981; Holloway 1982). Either way, the GM spectrum neglects the role of vortical motion, which can interact resonantly with waves to transfer wave energy downscale (Lelong & Riley 1991; Godeferd & Cambon 1994; Bartello 1995; Babin *et al.* 1997; Embid & Majda 1998). These authors have argued that resonant interactions between waves and vortical motion are more efficient than three-wave interactions at transferring wave energy. If the GM range is governed by resonant interactions and vortical motion is important, then the categories of three-wave interactions (elastic scattering, induced diffusion and

https://doi.org/10.1017/S0022112005007111 Published online by Cambridge University Press

parametric subharmonic instability) considered by McComas & Bretherton (1977) provide at best an incomplete understanding of the dynamics of the GM spectrum.

Numerical simulations of breaking internal waves have had mixed success at reproducing the observed energy spectrum. An early study by Orlanski & Cerasoli (1981) had insufficient resolution to reproduce realistic spectral slopes. Nevertheless, they anticipated the argument of Hines (1991) by showing that large-scale waves can be at equilibrium without being on the edge of instability, since growth in such waves can produce instability at small scales. Bouruet-Aubertot, Sommeria & Staquet (1996) performed two-dimensional simulations of a breaking standing wave at two different resolutions ($256^2$ and $512^2$). In both cases, spectra resembling (1.1) with $c = 0.1$ were obtained. In neither simulation was the buoyancy wavenumber $k_b$ resolved. In three dimensions, Carnevale, Briscolini & Orlandi (2001) forced a standing wave in a large-eddy simulation (LES) at $128^3$, with stratification chosen to resolve $k_b$. Downscale of $k_b$, they produced a spectral slope of $-5/3$; upscale, they reported slopes of around $-3$, but the spectra are quite bumpy. High-resolution LES (up to $512^3$) of stratified turbulence produce a clear spectral transition at $k_z \approx k_b$ (Yoshida, Ishihara & Kaneda 2002). Upscale of the transition, the spectrum is proportional to $k_z^{-2.3}$, which is significantly shallower than (1.1). There are few experimental studies of the energy spectrum produced by wave breaking because of the difficulty of obtaining measurements. Benielli & Sommeria (1996) forced a standing internal wave, and measured a frequency spectrum of the form $\omega^{-3}$ for $\omega > N$, which they transformed to $k_z^{-3}$ for $k_z > k_c$ using Taylor's hypothesis. The validity of this transformation is not clear.

In this paper, we use idealized numerical simulations to study stratified turbulence generated by randomly forced large-scale internal gravity waves. As in the numerical studies described above, we assume a homogeneous environment, with a constant background stratification and no shear. However, unlike past studies, we examine a wide range of stratifications, from weakly stratified turbulence to weakly interacting waves. We also consider the effect of vortical motion on the wave dynamics. We attempt to answer the following questions: Under what conditions, if any, does wave breaking in a uniformly stratified fluid produce the saturation spectrum (1.1)? How sensitive are the simulated spectra to changes in Reynolds number? What is the physical significance of the wavenumber $k_c$? What effect does the presence of vortical energy have on the spectrum of wave energy? In § 2, we introduce the equations of motion and describe the decomposition of the flow into wave and vortical parts. In § 3 we discuss our numerical approach. We then present simulations in which wave energy is forced alone at different stratifications (§ 4), at different resolutions (§ 5), and with different amounts of vortical forcing (§ 6). Conclusions are given in § 7.

## 2. Equations and wave–vortical mode decomposition

We take as our equations of motion the three-dimensional Boussinesq equations,

$$\frac{\partial \boldsymbol{u}}{\partial t} + \boldsymbol{u}\cdot\nabla\boldsymbol{u} = -\nabla p + b'\hat{\boldsymbol{z}} + \boldsymbol{F}_u + D_u(\boldsymbol{u}), \tag{2.1a}$$

$$\nabla\cdot\boldsymbol{u} = 0, \tag{2.1b}$$

$$\frac{\partial b'}{\partial t} + \boldsymbol{u}\cdot\nabla b' + N^2 w = F_{b'} + D_{b'}(b'), \tag{2.1c}$$

where $\boldsymbol{u} = u\hat{\boldsymbol{x}} + v\hat{\boldsymbol{y}} + w\hat{\boldsymbol{z}}$ is the velocity, $b' = -g\rho'/\rho_0$ (in the ocean) or $g\theta'/\theta_0$ (in the atmosphere) is the buoyancy, $\rho'$ and $\theta'$ are potential density and temperature

https://doi.org/10.1017/S0022112005007111 Published online by Cambridge University Press

perturbations, $\rho_0$ and $\theta_0$ are constant reference values, and $p$ is the dynamic pressure divided by $\rho_0$. The Brunt–Väisälä frequency $N$ is assumed to be constant. $D_u$ and $D_{b'}$ are dissipation operators, and $\boldsymbol{F}_u$ and $F_{b'}$ are forcing functions.

The strength of the stratification can be quantified by the vertical and horizontal Froude numbers $Fr_z = U/NL_z$ and $Fr_h = U/NL_h$, where $U$ is a characteristic horizontal velocity and $L_z$ and $L_h$ are characteristic vertical and horizontal length scales. We obtain $U/L_z$ and $U/L_h$ from the r.m.s. horizontal and vertical vorticity, and define

$$Fr_h = \frac{\sqrt{[\omega_z^2]}}{N}, \quad Fr_z = \frac{\sqrt{[\omega_x^2 + \omega_y^2]/2}}{N}, \tag{2.2}$$

where $[\cdot]$ denotes a volume average and $\boldsymbol{\omega} = \nabla \times \boldsymbol{u}$. We will see below that internal waves generate only small amounts of $\omega_z$, leading to artificially small values of $Fr_h$ (see table 3). We therefore use $Fr_z$ to characterize the strength of the stratification. Note that the prediction of Billant & Chomaz (2001) that $Fr_z \equiv 1$ applies to turbulence dominated by vortical motion, not internal waves.

The Ertel potential vorticity (PV) for (2.1) is $\Pi/\rho_0$, where

$$\Pi = \boldsymbol{\omega} \cdot \nabla b, \tag{2.3}$$

and $b = N^2 z + b'$. The PV can be used to separate a flow into vortical motion and internal waves, with the waves being defined to have no PV (Lelong & Riley 1991). In practice, however, the linear normal mode decomposition is often used. This procedure classifies the normal modes of the Fourier transform of (2.1) as either wave modes (fast) or vortical modes (slow) according to their linear frequencies. Following the notation of Bartello (1995), the normal mode amplitudes $(B_{\boldsymbol{k}}^{(+)}, B_{\boldsymbol{k}}^{(-)}, B_{\boldsymbol{k}}^{(0)})$ at wavevector $\boldsymbol{k}$ satisfy

$$\frac{\mathrm{d}B_{\boldsymbol{k}}^{(j)}}{\mathrm{d}t} + \mathrm{i}\lambda_{\boldsymbol{k}}^{(j)} B_{\boldsymbol{k}}^{(j)} = \sum_{\boldsymbol{k}=\boldsymbol{p}+\boldsymbol{q}} \sum_{r,s=\pm,0} \Gamma_{\boldsymbol{k}\boldsymbol{p}\boldsymbol{q}}^{jrs} B_{\boldsymbol{p}}^{(r)} B_{\boldsymbol{q}}^{(s)} + \hat{F}_{\boldsymbol{k}}^{(j)} + \hat{D}_{\boldsymbol{k}}^{(j)}, \tag{2.4}$$

where $j$ is 0, + or −. The 0 mode has linear frequency $\lambda_{\boldsymbol{k}}^{(0)} = 0$ and is called the vortical mode. The $\pm$ modes have internal wave frequencies $\lambda_{\boldsymbol{k}}^{(\pm)} = \pm\sigma_{\boldsymbol{k}}$, where

$$\sigma_{\boldsymbol{k}} = \frac{N k_h}{k}, \tag{2.5}$$

and are the two independent wave modes (upward and downward propagating) at $\boldsymbol{k}$.

The normal mode decomposition can be applied to any flow. However, because of the conservation of PV, it is most physically meaningful when it coincides with the PV decomposition. When do the two decompositions agree? PV has both linear and quadratic contributions in $(\boldsymbol{\omega}, b)$, i.e. $\Pi = \Pi_1 + \Pi_2$ where

$$\Pi_1 = N^2 \omega_z, \tag{2.6a}$$

$$\Pi_2 = \boldsymbol{\omega} \cdot \nabla b'. \tag{2.6b}$$

By the normal mode identities, the Fourier transform of $\Pi_1$ satisfies

$$\hat{\Pi}_{1\mathbf{k}} = N^2 k_h B_{\boldsymbol{k}}^{(0)} \tag{2.7}$$

(Bartello 1995), and so the vortical modes account for all of $\Pi_1$. As long as $\Pi_2 \ll \Pi_1$, the PV is approximately linear, and the normal mode decomposition approximates the PV decomposition. This approximation requires that $b$-surfaces be nearly horizontal. When vortical motion dominates, $\Pi_2/\Pi_1 \sim Fr_z^2$ and so the agreement between $\Pi$ and

https://doi.org/10.1017/S0022112005007111 Published online by Cambridge University Press

$\Pi_1$ is good when $Fr_z \ll 1$ (Waite & Bartello 2004). However, when waves dominate, the agreement is lost. The quadratic PV scales as $\max(WB/L_h^2, UB/L_hL_z)$ where $w \sim W$ and $b' \sim B$. The fact (from 2.1*b*) that $W \lesssim UL_z/L_h$, along with the assumption that $L_z \lesssim L_h$, implies that $\Pi_2 \lesssim UB/L_hL_z$. Following Riley & Lelong (2000) and setting $B \sim NU$ yields $\Pi_2 \lesssim NU^2/L_hL_z$. How does $\Pi_1$ scale? Internal waves generate $\omega_z$ only at first order in $Fr_z$ (Lelong & Riley 1991) and so $\omega_z \sim Fr_zU/L_h$. Therefore, $\Pi_1 \sim Fr_zN^2U/L_h$ and hence $\Pi_2/\Pi_1 \sim 1$. The simulations described below confirm this result. The linear PV is thus not a good approximation to $\Pi$ when waves dominate the flow. However, $\Pi_1$ and $\Pi_2$ are both small under these conditions. Despite its limitations, the normal mode decomposition is attractive because of its simplicity. As we will see below, its usefulness is demonstrated when the wave and vortical energy spectra are different from one another.

The wave/vortical decomposition breaks down when $k_h = 0$, since in this case all modes have zero frequency and no PV. These are the shear modes, which correspond to vertically sheared, horizontally uniform flow. The total energy $E = E^{(\pm)} + E^{(0)} + E^{(S)}$ is therefore the sum of the wave, vortical, and shear energy, defined as

$$E^{(\pm)} = \frac{1}{2}\sum_{k_h \neq 0} \left|B_{\boldsymbol{k}}^{(+)}\right|^2 + \left|B_{\boldsymbol{k}}^{(-)}\right|^2, \tag{2.8a}$$

$$E^{(0)} = \frac{1}{2}\sum_{k_h \neq 0} \left|B_{\boldsymbol{k}}^{(0)}\right|^2, \tag{2.8b}$$

$$E^{(S)} = \frac{1}{2}\sum_{k_h = 0} |\hat{u}_{\mathbf{k}}|^2 + |\hat{v}_{\mathbf{k}}|^2 + |\hat{b}_{\mathbf{k}}|^2/N^2. \tag{2.8c}$$

The nonlinear term in (2.4) is a sum over wavevector triads $\boldsymbol{k} = \boldsymbol{p} + \boldsymbol{q}$. Different classes of triads, involving different combinations of wave and vortical modes, contribute to the sum. In the limit of strong stratification, interactions are dominated by triads satisfying the resonance condition

$$\lambda_{\boldsymbol{k}}^{(j)} = \lambda_{\boldsymbol{p}}^{(r)} + \lambda_{\boldsymbol{q}}^{(s)}, \tag{2.9}$$

where $j, r$ and $s$ are 0 or $\pm$. The nonlinear evolution of the wave modes is governed by three classes of triads: three wave modes $(\pm, \pm, \pm)$, two wave modes and a vortical mode $(\pm, 0, \pm)$, and a single wave mode with two vortical modes $(\pm, 0, 0)$ (for a detailed discussion of the different classes of resonant triads, see Riley & Lelong 2000). Resonant $(\pm, \pm, \pm)$ triads have been well-studied, and much work has gone into interpreting the GM spectrum in the light of them (e.g. McComas & Bretherton 1977). However, in the presence of vortical motion, resonant $(\pm, 0, \pm)$ interactions can also affect the wave dynamics. The $(\pm, 0, 0)$ interactions, on the other hand, are never exactly resonant.

## 3. Numerical approach

### 3.1. *Methodology*

The equations of motion (2.1) were integrated in a periodic domain of size $2\pi$ for a variety of stratifications, resolutions and forcings. A pseudo-spectral code was employed with leapfrog time stepping and a Robert filter parameter of 0.04 (Asselin 1972). Aliasing errors were eliminated by truncating cylindrically at $k_h$, $|k_z| = k_t$, where $k_t = M/3$ for a spatial grid of size $M^3$ (we refer to $M$ as the resolution). Velocity and

https://doi.org/10.1017/S0022112005007111 Published online by Cambridge University Press

buoyancy were dissipated by cylindrical hyperviscosity and hyperdiffusion, with

$$D_u = \nu_h(-1)^{n+1}\nabla_h^{2n} + \nu_z(-1)^{n+1}\left(\frac{\partial}{\partial z}\right)^{2n}, \tag{3.1a}$$

$$D_b = \kappa_h(-1)^{n+1}\nabla_h^{2n} + \kappa_z(-1)^{n+1}\left(\frac{\partial}{\partial z}\right)^{2n}. \tag{3.1b}$$

We set the vertical and horizontal hyperviscosity and hyperdiffusion coefficients to $\nu$, and use $n=4$ (as in Bartello, Métais & Lesieur 1996). Hyperviscosity modifies the dissipation wavenumber $k_d = 1/l_d$, which becomes

$$k_d = \left(\frac{\epsilon}{\nu^3}\right)^{1/(6n-2)}. \tag{3.2}$$

In order to compare time-averaged quantities at different stratifications, statistically stationary Froude numbers are desirable, and so we have performed forced simulations. Expressed for the normal mode equation (2.4), our forcing has the form

$$\hat{F}_{\boldsymbol{k}}^{(j)} = \begin{cases} A^{(j)}(\boldsymbol{k})\, G_{\boldsymbol{k}}^{(j)}(t), & \boldsymbol{k} \in S_f \\ 0, & \boldsymbol{k} \notin S_f, \end{cases} \tag{3.3}$$

where $j$ is 0 or $\pm$. The $G_{\boldsymbol{k}}^{(j)}$ are complex Gaussian random processes with zero mean and a decorrelation time scale $\tau$, which is set to be $O(10)$ time steps to avoid exciting the leapfrog computational mode. $S_f$ is the set of forced wavevectors, which is centred around $k = (k_x^2 + k_y^2 + k_z^2)^{1/2} = \sqrt{2}\,k_f$ at an angle $\pm\phi_f$ from the horizontal:

$$S_f = \{\boldsymbol{k} \,|\, k_f - \Delta_k \leqslant k_r \leqslant k_f + \Delta_k; r = h, z; \cos\phi_f - \Delta_\phi \leqslant \cos\phi \leqslant \cos\phi_f + \Delta_\phi\}, \tag{3.4}$$

where $k_h = (k_x^2 + k_y^2)^{1/2}$, $\Delta_k = 1$ and $\Delta_\phi = 0.1$. We have chosen to force waves of relatively large scale and intermediate frequency (as in previous studies), and so we set $\phi_f = \pi/4$ and $k_f = 3$. $S_f$ therefore contains 60 independent wavevectors. The amplitude function $A^{(j)}(\boldsymbol{k})$ is quadratic in $\cos\phi$ and centred around $\cos\phi_f$:

$$A^{(j)}(\boldsymbol{k}) = 100a^{(j)}(\cos\phi_f + \Delta_\phi - \cos\phi)(\cos\phi - \cos\phi_f + \Delta_\phi). \tag{3.5}$$

Wave and vortical modes are forced by different amounts by choosing $a^{(+)}$, $a^{(-)}$ and $a^{(0)}$. We set $a^{(+)} = a^{(-)} \equiv a^{(\pm)}$, and so the two wave modes at every $\boldsymbol{k}$ are forced independently at the same amplitude.

Five sets of simulations will be presented in the following sections. Set 1 contains a single long simulation at a modest resolution of 90, in which only wave modes were forced. This simulation illustrates the difficulty we face in obtaining statistically stationary fields in forced stratified turbulence. In set 2 (the main simulations of this study), we forced waves at a higher resolution of 180 for eight different stratifications. The set of $N$ values was chosen to span the range of dynamically significant values from $Fr_z \gtrsim 1$ to $Fr_z \ll 1$. In set 3, we consider the sensitivity of our results to changes in Reynolds number $Re = (k_d/k_f)^{4/3}$: the simulations were repeated at lower resolutions of 90 and 128 and a higher resolution of 240. In a fourth set, a subset of the above simulations at $M = 180$ were repeated with the addition of vortical forcing. Different vortical forcing amplitudes were employed, with forcing ratios $R \equiv a^{(0)}/a^{(\pm)}$ of 1/8, 1/4, 1/2 and 1. Finally, we present a single high-resolution simulation with strong stratification and strong vortical forcing. The different values of $M$, $N$ and $R$ for each set are given in table 1.

https://doi.org/10.1017/S0022112005007111 Published online by Cambridge University Press

| Set | Resolution | $N$ | $R$ |
|---|---|---|---|
| 1 | 90 | 16 | 0 |
| 2 | 180 | 1/2, 1, 2, 4, 8, 16, 32, 64 | 0 |
| 3 | 90, 128, 240 | 1/2, 1, 2, 4, 8, 16, 32, 64 | 0 |
| 4 | 180 | 4, 8, 16, 32 | 1/8, 1/4, 1/2, 1 |
| 5 | 240 | 32 | 1 |

TABLE 1. Summary of the simulations to be discussed. The resolution is given by $M$, the number of spatial grid points in each direction. $N$ is the Brunt–Väisälä frequency and $R \equiv a^{(0)}/a^{(\pm)}$ is the relative amplitude of the vortical forcing.

| Resolution | $\Delta t$ | $\nu$ |
|---|---|---|
| 90 | 0.0039 | $5.0 \times 10^{-11}$ |
| 128 | 0.0027 | $3.0 \times 10^{-12}$ |
| 180 | 0.0019 | $2.0 \times 10^{-13}$ |
| 240 | 0.0014 | $2.0 \times 10^{-14}$ |

TABLE 2. Time steps and hyperviscosity coefficients used for different resolutions.

We used equal time steps and hyperviscosity coefficients for all simulations of a given resolution, and these quantities are listed in table 2. The $\nu$ values were chosen to maintain $k_d \approx 0.75\,k_t$, and so changes in resolution imply changes in $Re$. The forcing memory was $\tau = 0.019$, corresponding to between $5\Delta t$ (when $M = 90$) and $13\Delta t$ (when $M = 240$). The wave forcing amplitude was kept constant at $a^{(\pm)} = 0.072$, which has an associated time scale $T_f = (a^{(\pm)} k_f)^{-1/2} \approx 2$. All simulations were initialized with a small amount of Gaussian random seed energy with an isotropic spectrum centred around $k = k_f$. The initial energy was less than 1% of the levels at statistical stationarity.

Spectra of vortical and wave energy were computed by binning the normal mode variances into integer wavenumbers, i.e.

$$E_h^{(j)}(k_{h_i}) = \sum_{\boldsymbol{k}' \in I_h(k_{h_i})} \frac{1}{2}\left|B_{\boldsymbol{k}'}^{(j)}\right|^2, \quad E_z^{(j)}(k_{z_i}) = \sum_{\boldsymbol{k}' \in I_z(k_{z_i})} \frac{1}{2}\left|B_{\boldsymbol{k}'}^{(j)}\right|^2, \tag{3.6a, b}$$

where $j$ is 0 or $\pm$ and

$$I_h(k_{h_i}) = \{\boldsymbol{k}' \,|\, k_{h_i} - 1/2 \leqslant k_h' < k_{h_i} + 1/2\}, \tag{3.7a}$$

$$I_z(k_{z_i}) = \{\boldsymbol{k}' \,|\, k_{z_i} - 1/2 \leqslant |k_z'| < k_{z_i} + 1/2,\ k_h \neq 0\}. \tag{3.7b}$$

The spectra of shear and total energy are defined similarly.

### 3.2. *A very long simulation*

We began this work by performing a number of simulations at a low resolution of 90. Our aim was to proceed in the standard way: force until statistical stationarity, and then average various quantities in time. However, at certain stratifications we found a slow, systematic transfer of energy into a few modes, as encountered in previous studies (Smith & Waleffe 2002; Laval, McWilliams & Dubrulle 2003). This growth makes it impractical to reach stationarity, since very long integrations are required. The growing modes include shear modes (with $k_h = 0$, as in the previous studies) as well as others with small but non-zero $k_h$.

https://doi.org/10.1017/S0022112005007111 Published online by Cambridge University Press

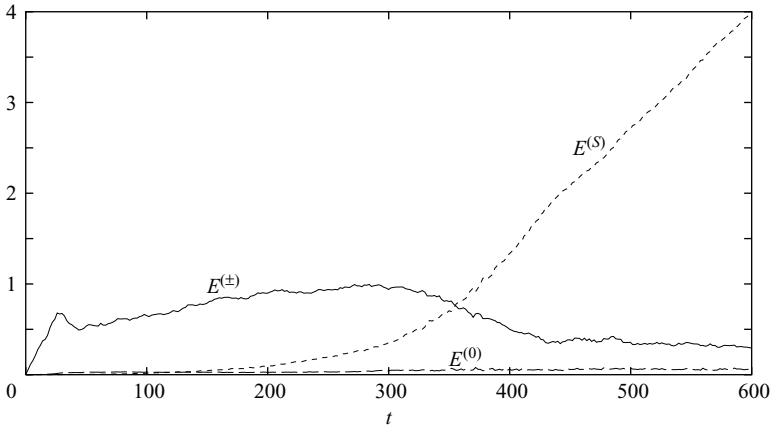



FIGURE 1. Time series of wave energy $E^{(\pm)}$, vortical energy $E^{(0)}$ and shear energy $E^{(S)}$ with $M = 90$, $N = 16$, and $R = 0$.

Run 1 is an example of a very long simulation which has not yet reached stationarity. The wave, vortical and shear energy are plotted against time in figure 1. This figure spans 300 forcing time scales $T_f$ and 5000 nonlinear turnover times defined (following Bartello & Warn 1996) as

$$n_t = \int_0^t [\boldsymbol{\omega}^2]^{1/2} \, \mathrm{d}t'. \tag{3.8}$$

From $t = 0$ to 50 ($n_t = 0$ to 200) the simulation spins up as expected: the total energy increases linearly as the forced modes are excited, until the energy spectrum fills out and dissipation balances the forcing. Statistical stationarity, however, does not follow. From $t = 50$ to 300 ($n_t = 200$ to 2000) the wave and shear energies grow. This growth is concentrated near $(k_h, |k_z|) = (1, 5)$ and $(0, 6)$. Around $t = 300$, $E^{(\pm)}$ drops off while $E^{(S)}$ continues to rise. By this time, the total shear energy is of the same order as the wave energy. Nonlinear interactions between wave and shear modes permit the energy trapped around $(k_h, |k_z|) = (1, 5)$ to be transferred to large $k_z$ and dissipated. Beyond $t = 450$ ($n_t = 3000$), the wave energy is stationary while the shear energy grows linearly. This regime can be understood simply: the shear modes form a stable vertically sheared horizontally uniform mean flow which absorbs the energy of small-amplitude perturbations injected at a constant rate.

The mechanism driving this slow, systematic growth is not fully understood (at least not at early times, when modes with $k_h \neq 0$ are not small perturbations around a stable horizontally uniform basic state), and more work is required to determine if it is relevant to atmospheric and ocean dynamics. In any case, long simulations like this one are beyond our capabilities at higher resolution. Our present interest is in the turbulence generated by wave breaking, which emerges at relatively early times. In the absence of statistical stationarity over long times, we restrict ourselves to the approximate stationarity occurring once the energy spectrum has filled out but before the growing modes dominate the flow (e.g. between $t \approx 40$ and 100 in this run). This is presumably the same approach followed unknowingly in forced simulations of stratified turbulence before Smith & Waleffe (2002) discovered the slow growth of the shear modes. The quasi-stationary range exists in all cases, although, as illustrated in this simulation, it can be quite short.

https://doi.org/10.1017/S0022112005007111 Published online by Cambridge University Press

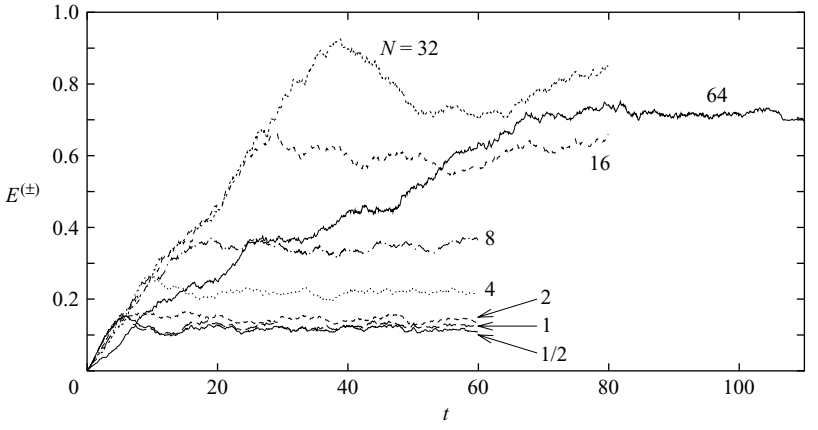



FIGURE 2. Time series of wave energy $E^{(\pm)}$ for $M = 180$, $1/2 \leqslant N \leqslant 64$ and $R = 0$.

| $N$ | $t_0$–$t_1$ | $n_{t_0}$–$n_{t_1}$ | $Fr_z$ | $Fr_h$ |
|---|---|---|---|---|
| 1/2 | 20–30 | 110–170 | 5.5 | 5.2 |
| 1 | 20–30 | 110–180 | 2.9 | 2.6 |
| 2 | 20–30 | 110–170 | 1.4 | 1.2 |
| 4 | 20–30 | 90–160 | 0.80 | 0.51 |
| 8 | 30–40 | 140–220 | 0.45 | 0.20 |
| 16 | 40–50 | 190–280 | 0.28 | 0.078 |
| 32 | 50–60 | 250–350 | 0.16 | 0.024 |
| 64 | 100–110 | 510–610 | 0.078 | 0.0054 |

TABLE 3. Intervals over which time averages are computed for set 2, given in terms of time $t$ ($t_0$–$t_1$) and nonlinear turnover time $n_t$ ($n_{t_0}$–$n_{t_1}$). The corresponding time-averaged vertical and horizontal Froude numbers are also provided.

## 4. Primary simulations

In our second set of simulations we forced wave modes alone at a resolution of 180 with eight different stratifications between $N = 1/2$ and 64. The initial linear growth rates of wave energy are independent of $N$ for $N \leqslant 32$ (time series of wave energy are plotted in figure 2), indicating that energy is injected at the same rate in each case. When $N \leqslant 1$, the time series are nearly identical. In the other simulations, the peak in wave energy occurs at later times for larger $N$. As the stratification is increased, nonlinear interactions are increasingly restricted to the resonant set, and the downscale transfer of energy is less efficient; the simulations therefore take longer to spin up. When $N = 64$, approximate stationarity is not reached until $t \approx 100$, but by this time, the slow growth in wave energy has begun for $N = 16$ and 32. No single interval exists which contains an approximately stationary range in every simulation, and so different averaging intervals have been used for each $N$ (see table 3). Each interval ($t_0$, $t_1$) has a length of 10, which corresponds to five forcing time scales and between 60 and 100 nonlinear turnover times. Unless otherwise specified, all quantities in the following sections have been averaged over these intervals. The shear energy, which is growing when $N \geqslant 4$, is never more than 2% of the total energy at these times.

Table 3 also lists time-averaged vertical and horizontal Froude numbers, as defined in (2.2). The Froude numbers provide a more meaningful characterization of the

https://doi.org/10.1017/S0022112005007111 Published online by Cambridge University Press

| $N$ | $L_z$ (atmosphere) | $L_z$ (ocean) |
|---|---|---|
| 1/2 | 200 m | 20 m |
| 1 | 300 m | 30 m |
| 2 | 700 m | 70 m |
| 4 | 1 km | 100 m |
| 8 | 2 km | 200 m |
| 16 | 4 km | 400 m |
| 32 | 6 km | 600 m |
| 64 | 10 km | 1 km |

TABLE 4. Characteristic vertical scales $L_z = U/(NFr_z)$ implied by the vertical Froude numbers in table 3 assuming $N = 0.01\,\mathrm{s}^{-1}$ and $U = 10\,\mathrm{m\,s}^{-1}$ in the atmosphere and $1\,\mathrm{m\,s}^{-1}$ in the ocean.

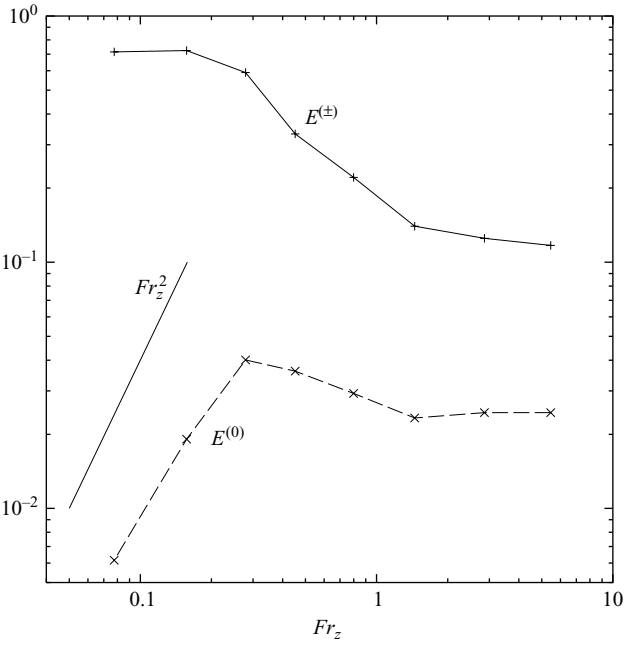



FIGURE 3. Total wave energy $E^{(\pm)}$ and vortical energy $E^{(0)}$ plotted against $Fr_z$ when $M = 180$ and $R = 0$.

stratification than the $N$, which are, to a certain extent, arbitrary. By identifying realistic values for $N$ and $U$, we can use the Froude numbers to determine the characteristic vertical length scales $L_z = U/(NFr_z)$ in each of our simulations. We assume typical values of $N = 0.01\,\mathrm{s}^{-1}$ and $U = 10\,\mathrm{m\,s}^{-1}$ in the atmosphere and $1\,\mathrm{m\,s}^{-1}$ in the ocean. The corresponding vertical scales for each simulation are given in table 4. This relationship between our simulations and the real atmosphere and ocean should be kept in mind but treated with caution. At our strongest stratifications, $L_z \sim 10$ km; at these scales, the Boussinesq approximation is no longer appropriate.

### 4.1. *Integrated quantities and length scales*

The total wave energy (plotted, along with the vortical energy, against $Fr_z$ in figure 3) depends on the spin-up time, which depends on the stratification. There is a transition

https://doi.org/10.1017/S0022112005007111 Published online by Cambridge University Press

around $Fr_z \approx 1$, below which the wave energy increases with increasing stratification. This transition is consistent with the emergence of a stratification-dependent spin-up time seen in figure 2. The vortical energy also increases with increasing stratification, until a second transition at $Fr_z \approx 0.3$. Further decrease in $Fr_z$ leads to a rapid drop in vortical energy. How do we understand the dependence of the vortical energy on stratification? Vortical modes are not forced directly, but are generated by nonlinear interactions with the wave modes. At weak stratifications, these interactions are strong, but the physical distinction between wave and vortical modes is lost. Waves become unstable and break, yielding small-scale turbulence which, even if not perfectly isotropic, projects onto all three normal modes. This process is visualized in figure 4, which shows snapshots of the $b$ field at different stratifications. The regions of static instability (or overturning, where $\partial b/\partial z < 0$ and vortical modes are generated) decrease in volume with rising $N$. As a result, the vortical energy is a decreasing fraction of the wave energy as $Fr_z$ is decreased over $0.3 \leqslant Fr_z \leqslant 1$, even though it increases in absolute value.

What happens when $Fr_z$ passes through 0.3 ($N = 16$)? Small patches of static instability are visible in figure 4 when $N = 16$ but not 32. We define $f_s$ to be the fraction of the spatial domain that is statically unstable (plotted against $N$ in figure 5*a*). When $N = 32$, $f_s$ is only intermittently non-zero; the time average and standard deviation are equivalent to just 3 and 6 unstable grid points, respectively, and so there is essentially no overturning. When $N = 64$, $f_s$ is identically zero at all times. The transition at $Fr_z \approx 0.3$ is from a regime (at larger $Fr_z$) in which wave breaking is resolved to one in which all static instability is inhibited by stratification and dissipation. The turbulent generation of vortical modes is suppressed in the absence of instability, and so $E^{(0)}$ falls off with decreasing $Fr_z$. It decreases like $Fr_z^{1.5}$ rather than the $Fr_z^2$ that one might expect from the work of Lelong & Riley (1991).

We have plotted $f_s$ against $N$ rather than $Fr_z$ because of the remarkable exponential dependence it displays when $N \leqslant 16$. The time average of $f_s$ is equivalent to the probability of static instability, i.e.

$$f_s = \int_{-\infty}^{-N} P_N(X)\,\mathrm{d}X, \tag{4.1}$$

where $P_N(X)$ is the probability density function (p.d.f.) of $X = \partial\theta'/\partial z$ (or, equivalently, $-\partial\rho'/\partial z$) at a given $N$. If the negative tails of $P_N(X)$ were exponential and independent of $N$, then the exponential decay of $f_s$ would follow. However, as seen in figure 5(*b*), the situation is more complicated. The tails are exponential (as seen in Métais & Lesieur 1992) but they are not independent of $N$. The negative tail moves in towards zero as $N$ increases to 2; when $N$ increases further, the tail moves out. Nevertheless, these changes in the p.d.f. are such that its integral from $-\infty$ to $-N$ remains exponentially dependent on $N$.

The total energy dissipation rate is

$$\epsilon = 2\nu\left(\int_0^{k_t} k_h^8 E_h(k_h)\,\mathrm{d}k_h + \int_0^{k_t} k_z^8 E_z(k_z)\,\mathrm{d}k_z\right), \tag{4.2}$$

and equals the energy injection rate at statistical stationarity. This quantity is only weakly dependent on $Fr_z$ when $Fr_z \geqslant 0.2$ (figure 6*a*). With $\epsilon$ we can compute the buoyancy and dissipation wavenumbers $k_b$ and $k_d$ which, along with $k_c$, are plotted in figure 6(*b*). This figure illustrates the two transitions noted above. As $Fr_z$ falls below 1, $k_b$ overtakes $k_d$, and no small-scale Kolmogorov inertial range is possible. We must

https://doi.org/10.1017/S0022112005007111 Published online by Cambridge University Press

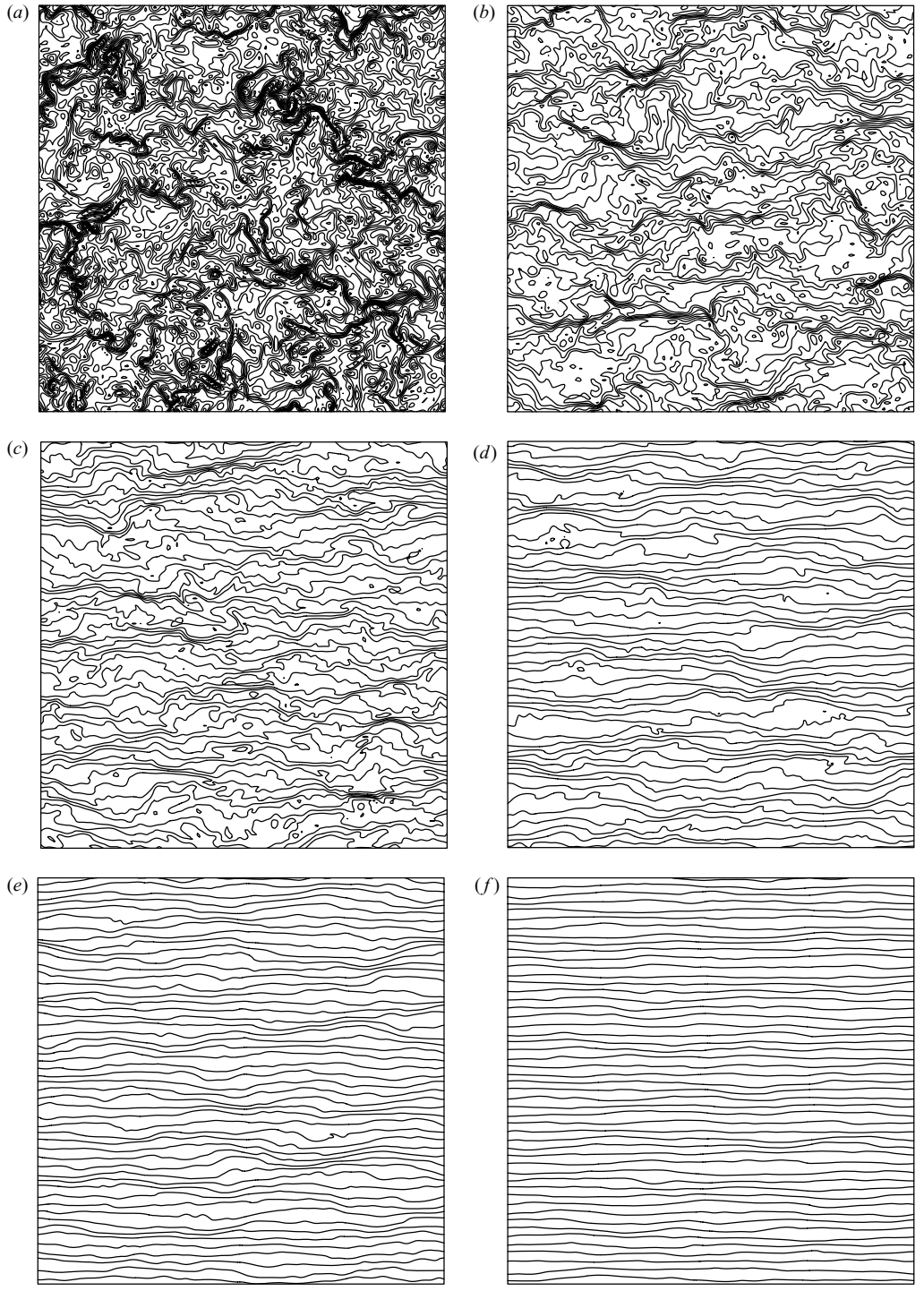



FIGURE 4. Vertical $(x, z)$ slices of total buoyancy $b = N^2 z + b'$ when $M = 180$, $R = 0$ and (*a*) $N = 1$, (*b*) $N = 2$, (*c*) $N = 4$, (*d*) $N = 8$, (*e*) $N = 16$ and (*f*) $N = 32$. The fields are shown at $t = t_1$ (see table 3). Contour intervals are $\Delta b = 2\pi N^2/50$, so that the background state has 50 contours in each case.

https://doi.org/10.1017/S0022112005007111 Published online by Cambridge University Press

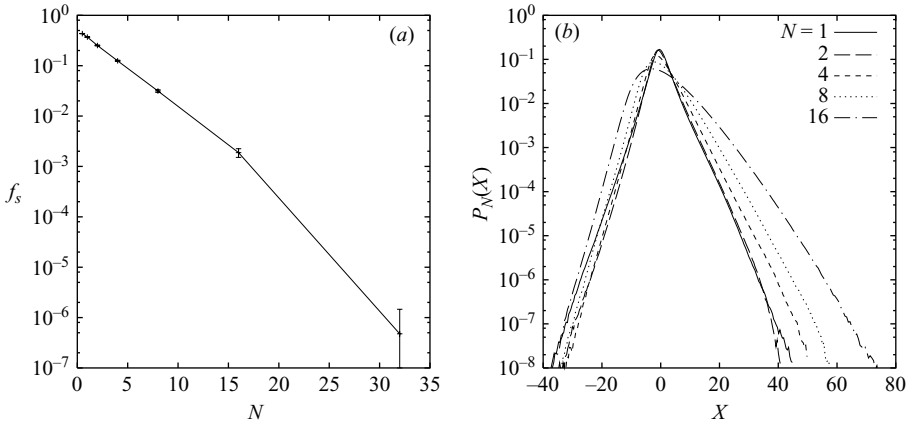



FIGURE 5. (*a*) The fraction $f_s$ of the spatial domain which is statically unstable plotted against $N$, with error bars indicating standard deviations (only non-zero values are plotted); and (*b*) p.d.f.s $P_N(X)$ of $X = \partial\theta'/\partial z$ for $N = 1$, 2, 4, 8 and 16, when $M = 180$ and $R = 0$.

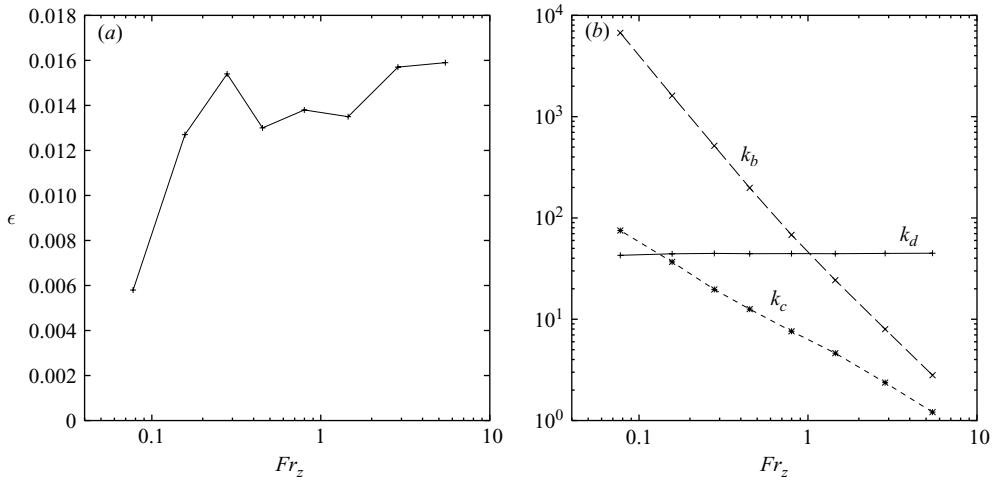



FIGURE 6. (*a*) Total energy dissipation rate $\epsilon$; and (*b*) the dissipation, buoyancy and overturning wavenumbers $k_d$, $k_b$ and $k_c$, plotted against $Fr_z$ when $M = 180$ and $R = 0$.

therefore check the sensitivity of these results to changes in Reynolds number (see § 5). Overturning and stratified turbulence persist even when $k_b > k_d$. As $Fr_z$ decreases below 0.3, $k_c$ approaches and surpasses $k_d$, and overturning is suppressed. Does $k_c$ have to be sufficiently smaller than $k_d$ to obtain overturning? We will argue below that it does, and so we refer to $k_c$ as the overturning wavenumber.

The identification of $u_{rms}/N$ with the overturning scale is reinforced by noting that it is approximately equal (to within 10% when $Fr_z < 1$) to $b'_{rms}/N^2$, where $b'_{rms}$ is the r.m.s. buoyancy. This quantity is related to the Thorpe scale, which is used by oceanographers to quantify the scale of overturning (Thorpe 1977). The Thorpe scale is the r.m.s. displacement required to rearrange a finite number of fluid elements to obtain a statically stable density profile. The length scale $b'_{rms}/N^2$ corresponds to the r.m.s. displacement required to obtain a state with no available potential energy, and so it provides us with an upper bound on the Thorpe scale.

https://doi.org/10.1017/S0022112005007111 Published online by Cambridge University Press

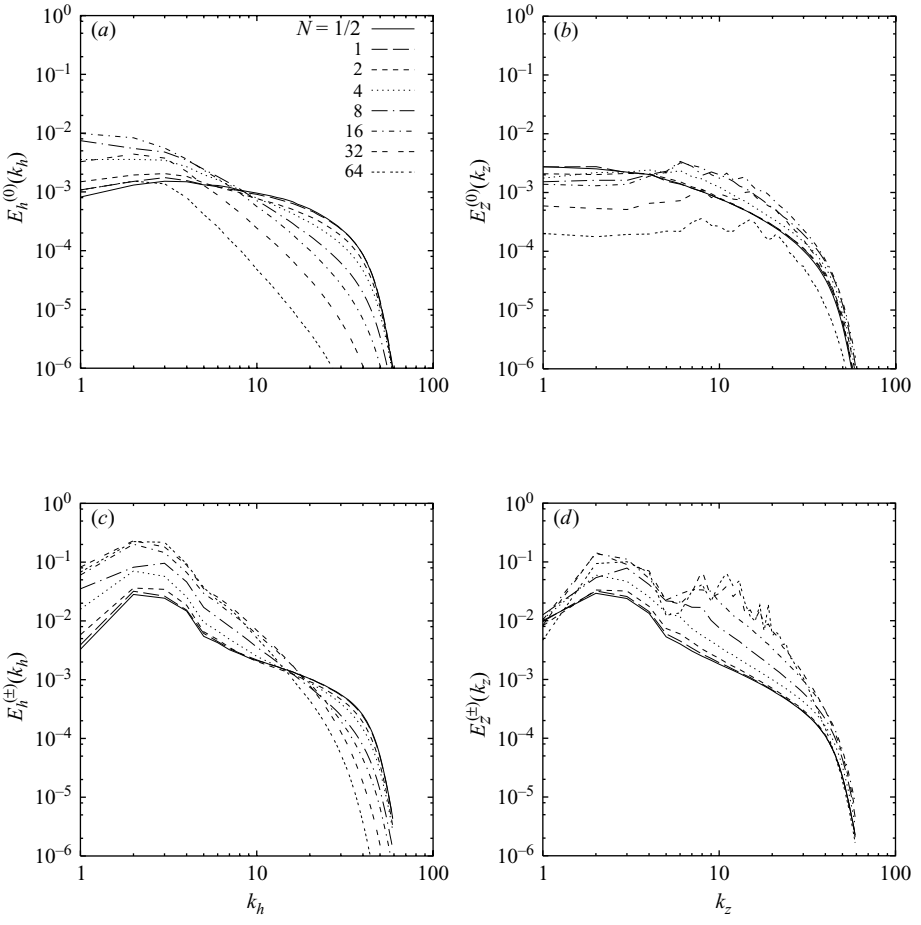



FIGURE 7. Horizontal and vertical wavenumber spectra of vortical energy (*a*) $E_h^{(0)}(k_h)$, (*b*) $E_z^{(0)}(k_z)$, and wave energy (*c*) $E_h^{(\pm)}(k_h)$ and (*d*) $E_z^{(\pm)}(k_z)$ when $M = 180$ and $R = 0$.

A remarkable feature of figure 6(*b*) is that the gap between the overturning and buoyancy wavenumbers widens with increasing stratification. This behaviour is inconsistent with the usual assumption that the overturning scale is proportional to $l_b$ (e.g. Itsweire, Helland & Van Atta 1986). When $Fr_z < 1$, the dependence of $k_b$ on $Fr_z$ may be affected by the fact that we are not resolving $k_b$, and so the $k_b$ scaling should be interpreted with caution. We will check the robustness of the $k_b$ scaling in § 5. If the widening range between $k_c$ and $k_b$ is real, it illustrates a major challenge facing numerical simulations of strongly stratified turbulence. To resolve $k_c$ and $k_b$ at a small Froude number requires significantly more resolution than employed here. For example, $k_b \approx 500$ when $Fr_z = 0.3$, and so a resolution of at least 1500 would be necessary. The best we can do with current resources is to resolve overturning but not the small isotropic scales, and explore whether the results are sensitive to resolution. As we will see below, they sometimes are.

### 4.2. *Spectral quantities*

The horizontal and vertical wavenumber spectra of vortical and wave energy have a strong dependence on stratification. The $k_h$ spectra of vortical energy (figure 7*a*)

https://doi.org/10.1017/S0022112005007111 Published online by Cambridge University Press

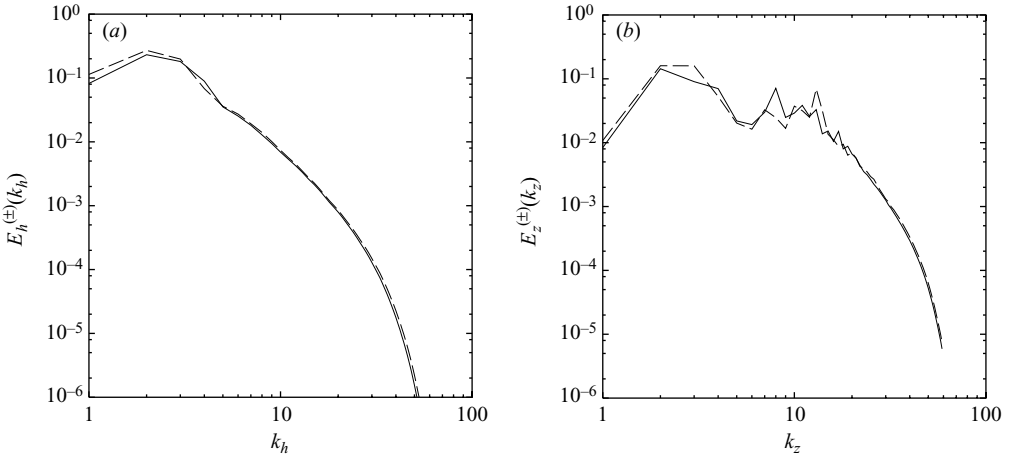



FIGURE 8. (*a*) Horizontal and (*b*) vertical wavenumber spectra of wave energy using the standard forcing (solid) and a restricted forcing (dashed) obtained by setting $\Delta_\phi = 0.001$ in (3.4) and (3.5). The $k_h$ spectrum is insensitive to the change in $S_f$, but the bumps in the $k_z$ spectrum are modified.

steepen rapidly as $N$ is increased beyond 4. The $k_z$ spectra of vortical energy (figure 7*b*) become increasingly flat as $N$ increases, but the flat range does not extend beyond $k_z \approx 20$. In Waite & Bartello (2004), we interpreted the flat range as resulting from decoupled layers of vortical motion. The vortical and wave energy spectra are parallel at large $k_z$ when $N \leqslant 16$, suggesting a breakdown of the utility of the normal mode decomposition at these scales. Note that the amplitudes of the vortical spectra drop rapidly as $N$ is increased beyond 16.

For the wave energy, the $k_h$ spectra (figure 7*c*) are shallower than $k_h^{-5/3}$ when $N \leqslant 2$ (i.e. when $k_b < k_d$), and they steepen rapidly at stronger stratifications. Our main interest, however, lies in the vertical wavenumber spectra of wave energy (figure 7*d*). When the stratification is weak ($N \leqslant 2$) the spectra are approximately independent of $N$ and have slopes around $-5/3$. As $N$ increases, the spectra become bumpier, steeper, and higher in amplitude. When $N = 4$, a small bump emerges at $k_z = 6$. It grows at higher stratifications and moves through $k_z = 8$ and 9 as $N$ is increased to 16. We have checked that these bumps have $k_h = 1$, and account for the systematic growth of wave energy observed at later times. The spectra are smooth beyond the bump, at least when $N \leqslant 16$. As $N$ is increased to 32, overturning is suppressed and the spectrum becomes extremely bumpy down to $k_z \approx 20$. Wave amplitudes cannot be limited by breaking in the absence of overturning, and so the energy spectrum is not saturated. Furthermore, at such small Froude numbers, resonant interactions are expected to dominate the nonlinear transfer. The intersection of the set of resonant triads with the finite set of modes in our simulations is relatively small, and so bumpy spectra are produced. These bumps are sensitive to the details of the forcing, as seen in figure 8. This figure plots the wave energy spectra at $N = 32$ from figure 7 along with those obtained with a slightly restricted set of forced modes (with $\Delta_\phi = 0.001$ and $a^{(\pm)} = 0.11$).

How well do the spectral slopes and amplitudes in figure 7(*d*) agree with the saturation spectrum (1.1)? Slopes of $E_z^{(\pm)}(k_z)$ (measured by a least-squares fit to a power law over the range $10 \leqslant k_z \leqslant 30$) are listed in table 5 along with the spectral spread (the r.m.s. distance between the spectrum and the best-fit power law). The

https://doi.org/10.1017/S0022112005007111 Published online by Cambridge University Press

| $N$ | Slope | Spread | $N$ | Slope | Spread |
|---|---|---|---|---|---|
| 1/2 | −1.7 | $5.0 \times 10^{-5}$ | 8 | −2.3 | $1.2 \times 10^{-4}$ |
| 1 | −1.7 | $5.2 \times 10^{-5}$ | 16 | −2.8 | $4.3 \times 10^{-4}$ |
| 2 | −1.8 | $3.9 \times 10^{-5}$ | 32 | −3.2 | $5.6 \times 10^{-3}$ |
| 4 | −1.9 | $3.4 \times 10^{-5}$ | 64 | −3.7 | $9.7 \times 10^{-3}$ |

TABLE 5. The slopes $m$ of $E_z^{(\pm)}(k_z)$, measured by a least-squares fit to $ak_z^m$ over the range $10 \leqslant k_z \leqslant 30$. The spread is the r.m.s. difference between the spectrum and the best fit over this range of $k_z$.

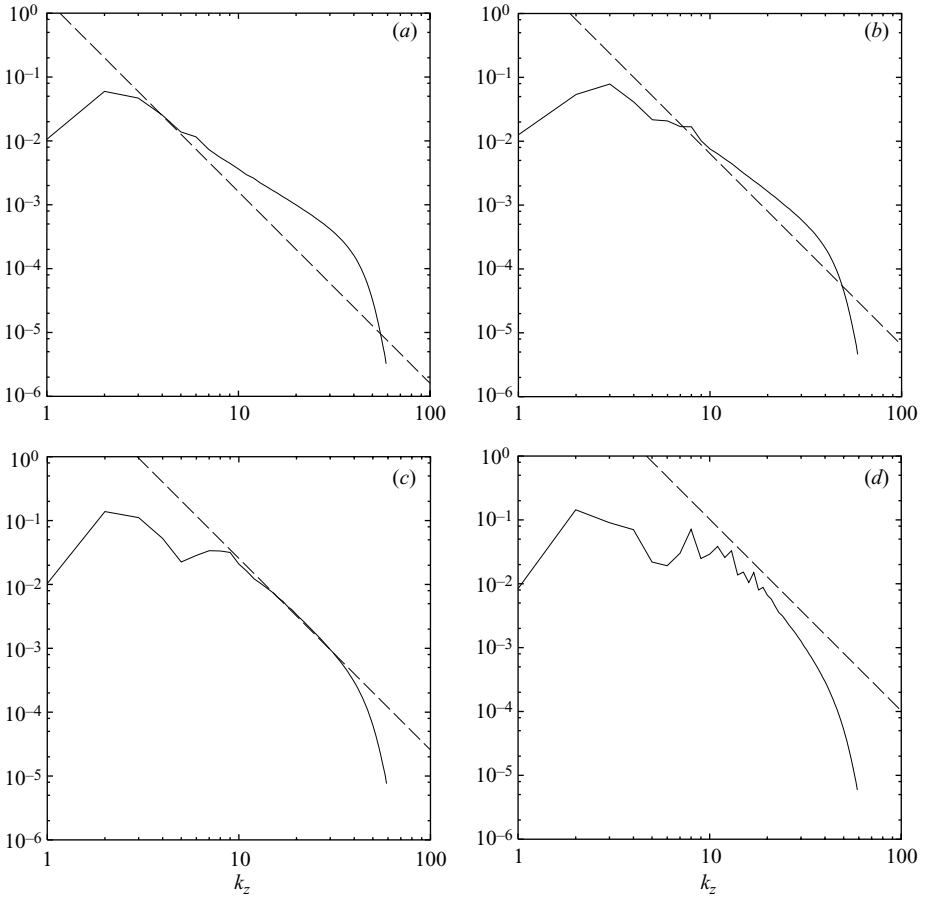



FIGURE 9. Vertical wavenumber spectra of wave energy (solid), along with the hypothetical saturation spectrum $0.1\,N^2\,k_z^{-3}$ (dashed), for (*a*) $N = 4$, (*b*) $N = 8$, (*c*) $N = 16$ and (*d*) $N = 32$ when $M = 180$ and $R = 0$.

spectra steepen as $N$ increases, slowly at first, then rapidly. The slope passes through $-3$ as $N$ goes from 16 to 32, just before overturning is suppressed and the long bumpy range emerges. The spread jumps by more than an order of magnitude as the spectrum is overwhelmed by bumps. As for the amplitudes, figure 9 plots the spectra for $4 \leqslant N \leqslant 32$ along with the corresponding saturation spectra with $c = 0.1$ (as in Bouruet-Aubertot *et al.* 1996). The growth in amplitude with $N$ is visibly slower than

https://doi.org/10.1017/S0022112005007111 Published online by Cambridge University Press

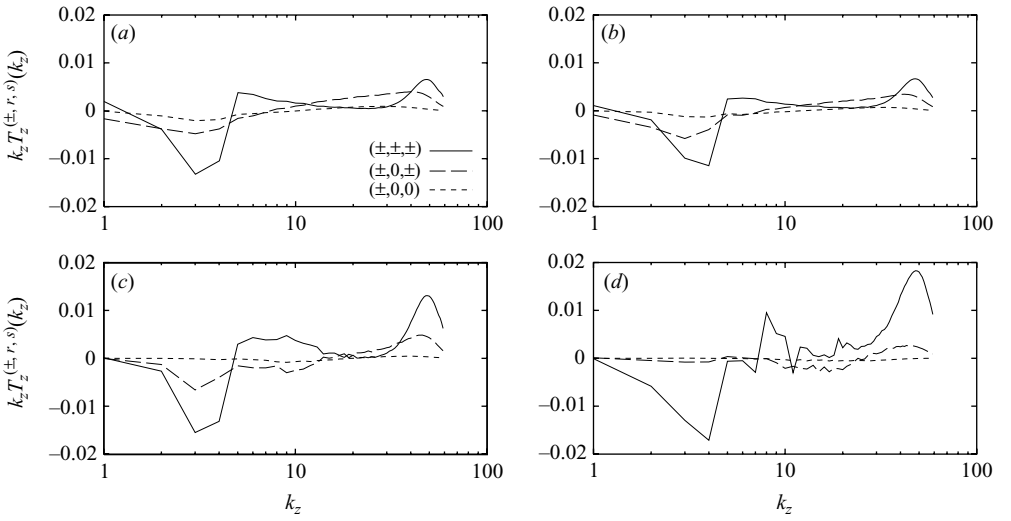



FIGURE 10. Vertical wavenumber spectra of wave energy transfer, decomposed into contributions from $(\pm,\pm,\pm)$, $(\pm,0,\pm)$ and $(\pm,0,0)$ triads, for (*a*) $N=1/2$, (*b*) $N=2$, (*c*) $N=8$, and (*d*) $N=32$, when $M=180$ and $R=0$.

$N^2$. As $N$ increases from 4 to 32, the amplitude (taken to be the value of the spectrum at $k_z=15$) grows instead like $N^{1.1}$. While this is a serious departure from (1.1), it is better than some atmospheric observations (e.g. Nastrom *et al.* 1997). Interestingly, the amplitudes and slopes in our simulations agree best with the saturation spectrum at the same stratification ($N=16$).

Transfer functions of wave and vortical energy are given by

$$T^{(j)}(\boldsymbol{k}) = 2\,\mathrm{Re} \sum_{\boldsymbol{k}=\boldsymbol{p}+\boldsymbol{q}} \sum_{r,s=\pm,0} \Gamma^{jrs}_{\boldsymbol{kpq}} B^{(j)^*}_{\boldsymbol{k}} B^{(r)}_{\boldsymbol{p}} B^{(s)}_{\boldsymbol{q}}, \tag{4.3}$$

where $j$ is 0 or $\pm$ and $*$ denotes the complex conjugate. Transfer spectra are defined analogously to the energy spectra. By restricting the summation over $r$ and $s$, we can define the contributions to the energy transfer of different classes of triads, i.e.

$$T^{(j)}(\boldsymbol{k}) = T^{(j,\pm,\pm)}(\boldsymbol{k}) + T^{(j,0,\pm)}(\boldsymbol{k}) + T^{(j,0,0)}(\boldsymbol{k}), \tag{4.4}$$

where $j$ is 0 or $\pm$ (in practice, the transfer decomposition is computed by filtering out wave or vortical modes before computing the nonlinear term). For example, $T^{(\pm,0,\pm)}(\boldsymbol{k})$ represents the transfer of wave energy at $\boldsymbol{k}$ due to triads of two wave modes and a vortical mode, and $T^{(0,\pm,\pm)}(\boldsymbol{k})$ is the transfer of vortical energy at $\boldsymbol{k}$ due to the same class of triads. Decomposed $k_z$ spectra of wave energy transfer are plotted in figure 10. The transfer is naturally dominated by $(\pm,\pm,\pm)$ interactions, since no vortical energy is forced. However, when $N \leqslant 2$, $(\pm,0,\pm)$ triads are important at intermediate $k_z$. At these weak stratifications, the normal modes lose their dynamical distinction, and the turbulent cascade projects onto all classes of triads. When $N=8$, a broad peak is visible in the $(\pm,\pm,\pm)$ transfer around $k_z=9$. This injection of energy is only partially balanced by a downscale transfer via $(\pm,\pm,0)$ interactions. As a result, the wave energy in these modes grows slowly. The transfer spectrum at $N=32$, like the energy spectrum, is very bumpy. The $(\pm,0,\pm)$ interaction plays only a minor role in this case, due to the small amount of vortical energy present. We will explore the role of this interaction in the presence of greater amounts of vortical energy below.

https://doi.org/10.1017/S0022112005007111 Published online by Cambridge University Press

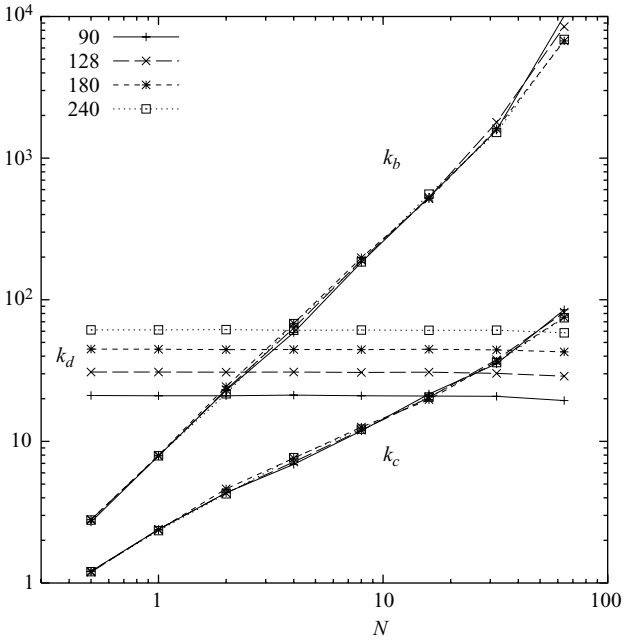



FIGURE 11. The dissipation, buoyancy and overturning wavenumbers $k_d$, $k_b$ and $k_c$ plotted against $N$ when $R = 0$ and $M = 90$, 128, 180 and 240.

## 5. Sensitivity to Reynolds number

The nonlinear interactions of stratified turbulence are less local in wavenumber than those of unstratified turbulence. The energy transfer at large and intermediate scales may therefore involve interactions with small scales, and so the energy spectrum may be dependent on the degree to which small scales are resolved (i.e. on $Re$). Given the impracticality of resolving an inertial range below the buoyancy scale at every Froude number considered here, we have instead examined the sensitivity of the results in § 4 to changes in $Re$. We have performed an additional set of simulations at three different Reynolds numbers, using resolutions of 90, 128 and 240 (set 3). When $M = 90$ and 128, the methodology was exactly analogous to that discussed in § 4. Simulations with $M = 240$, on the other hand, were first spun up at a resolution of 180 using the simulations of set 2. The resolution was increased to 240 at time $t = t_0 - 10$, and averaged as above from $t_0$ to $t_1$. Our four resolutions have Reynolds numbers of 13 ($M = 90$), 22 ($M = 128$), 36 ($M = 180$) and 55 ($M = 240$), which are admittedly small. By choosing $k_f = 3$ we avoid forcing the gravest mode, but at the cost of a reduced $Re$ compared with what could be obtained with a smaller $k_f$. Since our $Fr_z$ is calculated using the vorticity variance, increasing $M$ at a given $N$ has the effect of increasing $Fr_z$. As a result, we use $N$ to distinguish stratifications in this section.

### 5.1. *Length scales and instability*

In figure 11, we plot the dissipation, buoyancy and overturning wavenumbers for all four resolutions. The dissipation wavenumber $k_d$, unlike $k_b$ and $k_c$, depends significantly on the resolution. The dependence of $k_b$ and $k_c$ on Froude number appears to be robust to changes in Reynolds number. Furthermore, there is a relationship between the ratio of $k_c/k_d$ and the emergence of overturning. Compare figure 11 with figure 12($a$), which plots $f_s$ against $N$ for each $Re$. Apart from two

https://doi.org/10.1017/S0022112005007111 Published online by Cambridge University Press

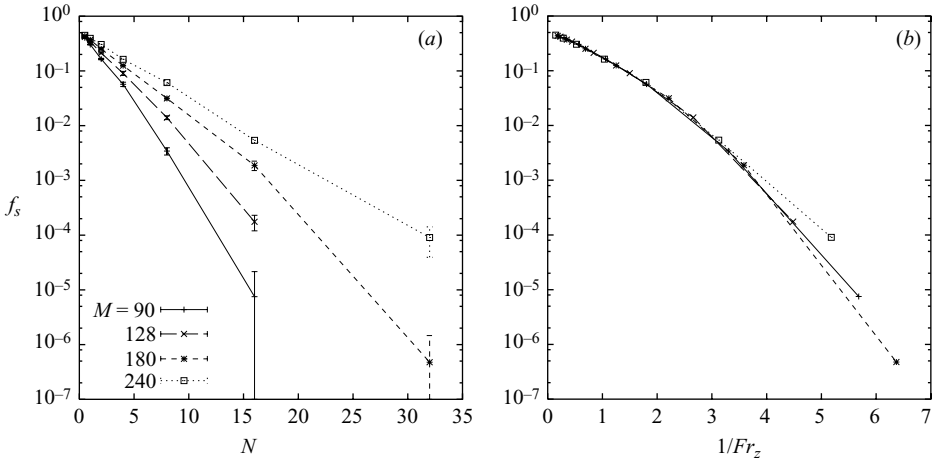



FIGURE 12. The fraction $f_s$ of the spatial domain which is statically unstable plotted against (*a*) $N$ and (*b*) $1/Fr_z$ when $R = 0$ and $M = 90$, 128, 180 and 240. Only non-zero values are plotted. The error bars in (*a*) are computed using standard deviations.

exceptions, there is significant overturning when $k_c < k_d$, and no overturning at any time when $k_c > k_d$. In two cases, $k_c \approx k_d$ and only marginal overturning is generated (i.e. $f_s$ is only intermittently non-zero). When $N = 16$ and $M = 90$, $k_c/k_d = 1.0$ and the time average and standard deviation of $f_s$ correspond to just 5 and 10 unstable grid points, respectively. When $N = 32$ and $M = 180$, $k_c/k_d = 0.83$ and there is an average of just three unstable grid points, with a standard deviation of 6 (as seen above). These results appear to justify our reference to $k_c$ as the overturning wavenumber: $k_c/k_d < 0.8$ is necessary and sufficient for the generation of static instability in our simulations. Having $k_b < k_d$, on the other hand, is not necessary.

As we saw above, $f_s$ decreases exponentially with increasing $N$, but the rate of decay drops with increasing $Re$ as finer scales of overturning are resolved. However, $N$ is dimensional, and is therefore not necessarily the most appropriate variable to use in this context. In figure 12(*b*) we instead plot $f_s$ against $1/Fr_z$, a dimensionless $N$. The curves are no longer exponential but, remarkably, they have collapsed onto one another. Both $Fr_z$ and $f_s$ change with $Re$ at a given stratification, but these changes combine to make the dependence of $f_s$ on $Fr_z$ independent of $Re$.

### 5.2. *Energy spectra*

The vertical wavenumber spectra of wave energy (plotted for all resolutions in figure 13) are naturally dependent on $Re$ in the dissipation range, but are not necessarily so at smaller $k_z$. The spectra are independent of $Re$ along $k_z < 20$ at low stratifications ($N \leqslant 4$). When $N = 8$, however, this independence is lost: as $M$ goes from 90 to 128, the spectrum gets shallower. The increase from $M = 180$ to 240 has a more subtle effect on the spectrum, which appears to have nearly converged with a slope of around $-2.1$. The convergence is less convincing when $N = 16$, as the $M = 240$ spectrum is noticeably shallower than the others. The agreement between the simulated spectrum and (1.1) when $N = 16$ and $M = 180$ (figure 9*c*) was therefore somewhat fortuitous, since the spectrum was steepened towards a slope of $-3$ by a lack of resolution. Figure 13(*e*) suggests that, when $N = 16$, $E_z^{(\pm)}(k_z)$ will be no steeper than $k_z^{-2.5}$ as $Re \to \infty$. When $N = 32$, the spectrum gets shallower with increasing resolution, without converging.

https://doi.org/10.1017/S0022112005007111 Published online by Cambridge University Press

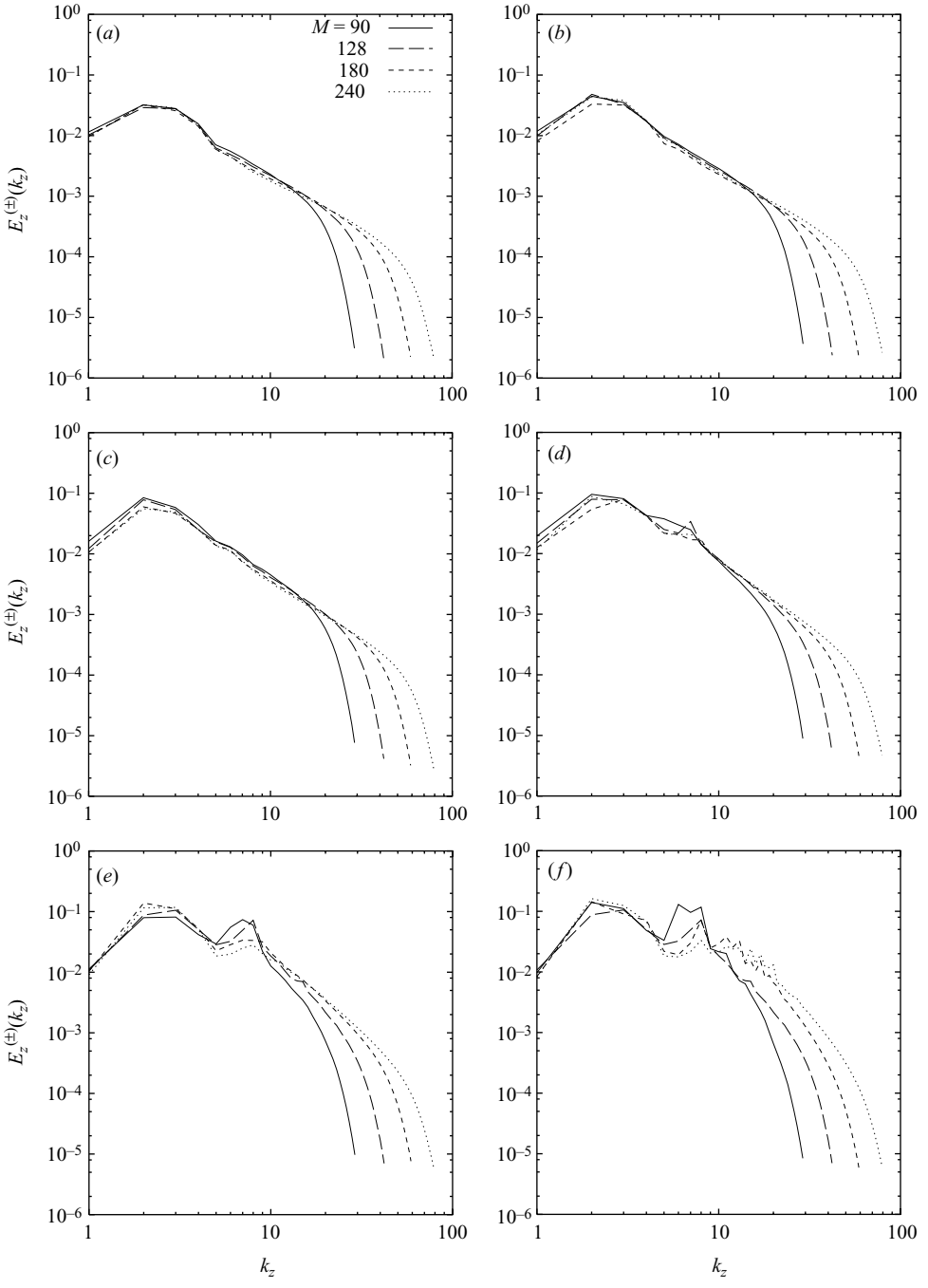



FIGURE 13. Vertical wavenumber spectra of wave energy at resolutions of 90, 128, 180 and 240 for $R = 0$ and (*a*) $N = 1$, (*b*) $N = 2$, (*c*) $N = 4$, (*d*) $N = 8$, (*e*) $N = 16$ and (*f*) $N = 32$.

How much resolution is necessary (i.e. how large must $k_b$ be) to obtain spectra which are independent of $Re$ outside the dissipation range? It would appear that it is not necessary to have $k_d > k_b$, as the simulations with $N = 4$ indicate. It is, however, necessary to have $k_d > k_c$, but to what extent? All of the simulations with $N = 4$ have

https://doi.org/10.1017/S0022112005007111 Published online by Cambridge University Press

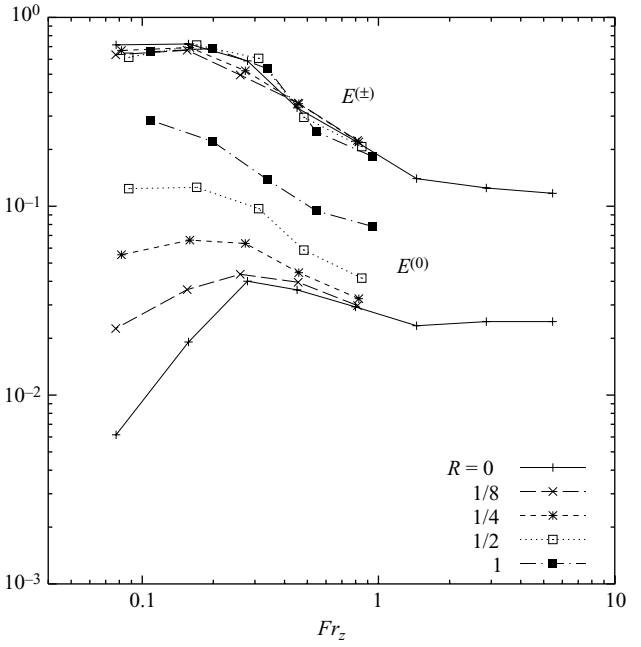



FIGURE 14. Wave and vortical energy plotted against $Fr_z$ for $R = 0$, 1/8, 1/4, 1/2 and 1 when $M = 180$.

$k_d > 3.1\,k_c$, and have converged with respect to increasing $Re$. When $N = 8$, $M = 128$ yields $k_d \approx 2.5\,k_c$ which is insufficient for convergence; $M = 240$, on the other hand, gives $k_d \approx 4.9\,k_c$ which appears to be enough. When $N = 16$, none of the simulations have sufficient resolution, and $k_d < 3.0\,k_c$ in each. So as a preliminary result, we may say that the overturning scale $l_c = 1/k_c$ must exceed the dissipation scale $l_d = 1/k_d$ by at least a factor of three in order for the spectra to be insensitive to changes in $Re$. This claim should be verified at higher resolution.

## 6. Sensitivity to vortical forcing

Vortical motion coexists with internal waves in the atmosphere and ocean, and because of the $(\pm, 0, \pm)$ interaction, its presence can affect the nonlinear transfer (and hence the energy spectrum) of the waves. No vortical modes were forced in the above simulations, and so this interaction did not play a significant role. In this section, we examine the extent to which the addition of vortical mode forcing modifies the above spectra of wave energy. We have repeated our simulations with $4 \leqslant N \leqslant 32$ at a resolution of 180 with four non-zero vortical mode forcing amplitudes $a^{(0)}$. The corresponding vortical/wave forcing ratios $R = a^{(0)}/a^{(\pm)}$ take the values 1/8, 1/4, 1/2 and 1 (set 4; see § 3.1). Quantities were averaged over the same intervals used above, and the resulting $Fr_z$ values were not significantly different from those obtained when $R = 0$ (table 3).

The time-averaged wave and vortical energy are plotted against $Fr_z$ for each $R$ in figure 14. The vortical energy depends on $R$ as well as stratification. When $R \leqslant 1/4$, the vortical forcing is weak; vortical energy decreases as $Fr_z$ is decreased below 0.3 by the mechanism described in § 4.1. When $R \geqslant 1/2$, however, the vortical forcing is sufficiently strong that the vortical energy increases with increasing stratification,

https://doi.org/10.1017/S0022112005007111 Published online by Cambridge University Press

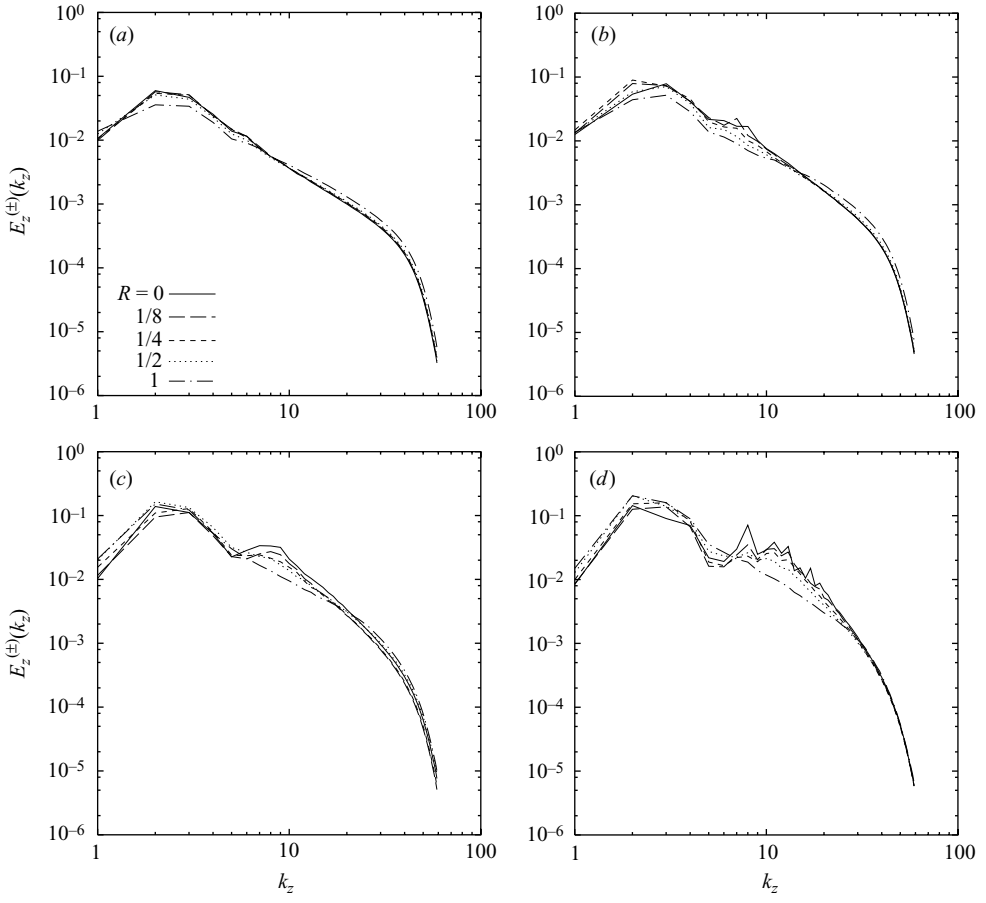



FIGURE 15. Vertical wavenumber spectra of wave energy for $R = 0$, 1/8, 1/4, 1/2 and 1 when $M = 180$ and (*a*) $N = 4$, (*b*) $N = 8$, (*c*) $N = 16$ and (*d*) $N = 32$.

which also occurs when vortical modes alone are forced (Waite & Bartello 2004). The presence of vortical energy has only a weak effect on the amount of wave energy at stationarity. The energy-containing range of the spectrum (around $k = k_f$) is insensitive to $R$, as we will see next.

The vertical wavenumber spectra of wave energy obtained with different amounts of vortical forcing are shown in figure 15. When $N = 4$, the spectrum is insensitive to the presence of vortical energy, except for the strongest case ($R = 1$) in which the large wavenumbers are increased in amplitude. This stratification is weak, and so the distinction between wave and vortical modes is blurred; increasing $R$ raises the dissipation rate, which produces a higher-amplitude spectrum at large $k_z$. We see this feature again when $N = 8$. When $N \geqslant 8$, however, the vortical modes have another important effect: the bumps in the spectra get smaller as $R$ increases, and essentially disappear when $R = 1$. This effect is most striking when $N = 32$. When $R = 1$, the bumpy range (which extends to $k_z \approx 20$ when $R = 0$) is gone, and the spectrum is a power law with a slope of approximately $-2.1$.

The wave energy spectra are smoothed by the presence of vortical energy through the $(\pm, 0, \pm)$ interaction. Figure 16 shows the vertical wavenumber transfer spectra of wave energy in the most strongly stratified case ($N = 32$) for each non-zero

https://doi.org/10.1017/S0022112005007111 Published online by Cambridge University Press

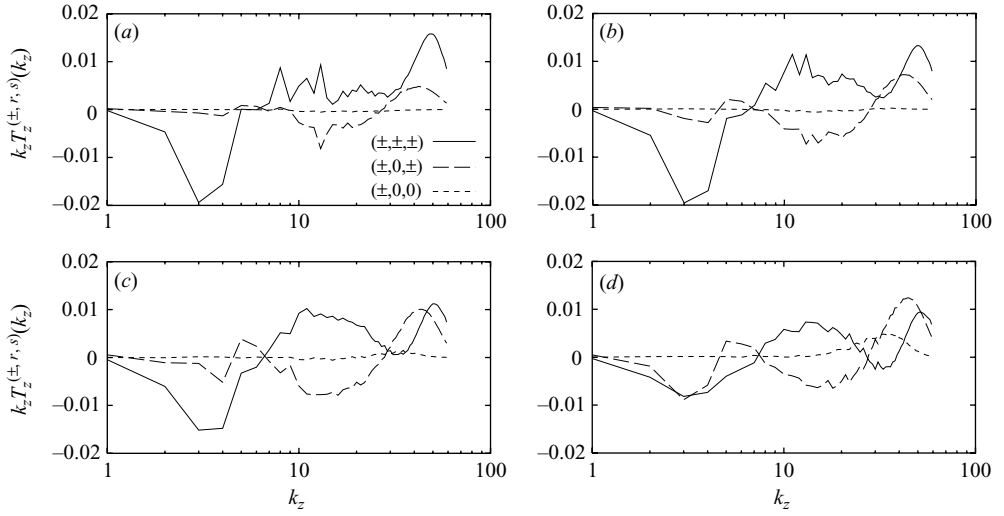



FIGURE 16. Vertical wavenumber spectra of wave energy transfer, decomposed into contributions from $(\pm,\pm,\pm)$, $(\pm,0,\pm)$ and $(\pm,0,0)$ triads, for (*a*) $R=1/8$, (*b*) $R=1/4$, (*c*) $R=1/2$ and (*d*) $R=1$, when $N=32$ and $M=180$.

vortical forcing amplitude. When $R=0$, the transfer is dominated by three-wave interactions, which remove wave energy from the forced modes and inject it into a few intermediate $k_z$ values (the bumps in the energy spectrum) and the dissipation range (see figure 10*d*). When $R>0$, the presence of vortical energy allows the $(\pm,0,\pm)$ interaction to remove energy from the bumpy range and send it downscale. As $R$ is raised, there is an increasing balance between the injection of energy by $(\pm,\pm,\pm)$ interactions at intermediate wavenumbers, and its removal by $(\pm,0,\pm)$ interactions. No bumps remain when $R=1$.

The energy spectrum which results from this balance between $(\pm,\pm,\pm)$ and $(\pm,0,\pm)$ interactions is smooth, but it appears to be sensitive to changes in $Re$. We performed an additional simulation with $N=32$ at a resolution of 240 (run 5). The resulting $k_z$ spectrum of wave energy is shallower than that obtained with $M=180$, and resembles $k_z^{-5/3}$ (figure 17). There is essentially no overturning generated ($f_s$ has a time average of $3\times10^{-6}$), and so this regime is very different from the strongly turbulent environment in which Alisse & Sidi (2000) also obtained a $k_z^{-5/3}$ spectrum. Indeed, our rough estimate above gives a characteristic vertical scale of this regime of $O(10)$ km, while the observations of Alisse & Sidi (2000) were from 1 to 10 m (see table 4). The vortical energy spectrum in this simulation is approximately flat, and so the total energy spectrum is actually much shallower than $k_z^{-5/3}$ (figure 17).

## 7. Conclusions

By performing simulations of randomly forced internal waves in a uniformly stratified Boussinesq fluid, we have attempted to reproduce the saturation spectrum $E_z(k_z)=c\,N^2k_z^{-3}$ observed in the atmosphere and ocean. Our simulated spectra steepen and increase in amplitude with increasing stratification. However, they are generally shallower than $k_z^{-3}$, and their amplitudes increase like $N^{1.1}$ rather than $N^2$. In the most strongly stratified simulation that resolves wave breaking ($Fr_z\approx0.3$), the spectrum appears to agree well with $0.1\,N^2k_z^{-3}$, but the agreement is spurious. At

https://doi.org/10.1017/S0022112005007111 Published online by Cambridge University Press

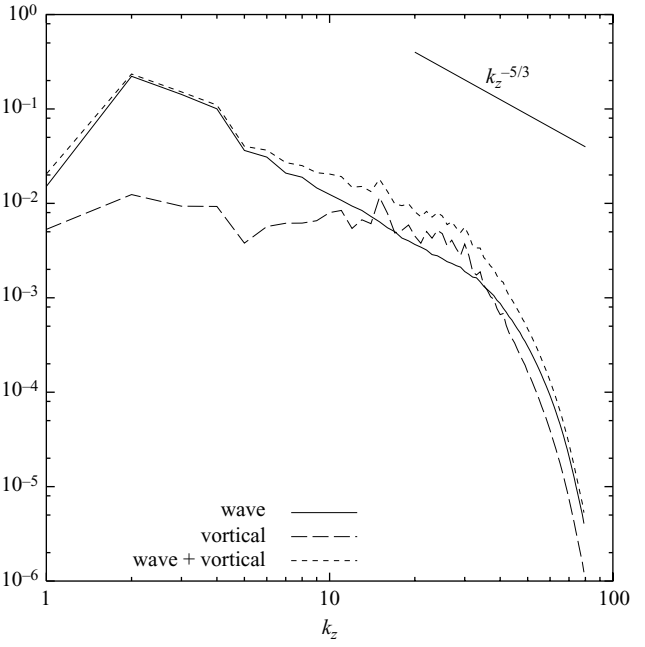



FIGURE 17. Vertical wavenumber spectra of wave, vortical and total energy for $N = 32$, $R = 1$ and $M = 240$ (run 5).

this stratification, the spectrum is sensitive to changes in Reynolds number, and gets shallower as $Re$ increases; in the limit $Re \to \infty$, it will be no steeper than $k_z^{-2.5}$. These results recall the findings of Nastrom *et al.* (1997), who observed similar departures in amplitude and slope from the saturation spectrum in the atmosphere, especially in the troposphere. Nevertheless, our results are inconsistent with most of the reported observations in the stratosphere as well as the ocean. Perhaps this inconsistency should not be surprising, since our approach is limited by the use of a constant $N$ and the Boussinesq approximation. The Brunt–Väisälä frequency varies significantly in the thermocline where most observations are made in the ocean, and the Boussinesq approximation breaks down over large vertical scales in the atmosphere. Indeed, non-Boussinesq effects in the atmosphere cause vertically propagating waves to grow in amplitude, which is an important part of the saturation process. We might represent this growth in the current homogeneous Boussinesq framework by steadily forcing a broad spectrum of waves down to $k_z = N/u_{rms}$. Ultimately, however, the generation of the observed spectrum should be studied in a more realistic atmosphere or ocean model. The effects of rotation on the results presented here should also be considered.

The length scale $l_c = u_{rms}/N$ is the overturning scale in our simulations: static instability is present only when $l_c$ is larger than the dissipation scale. At sufficiently strong stratifications, $l_c$ is smaller than $l_d$, no overturning is generated, and (when only waves are forced) three-wave interactions dominate the flow. Our simulations yield a bumpy spectrum in this limit which does not resemble the Garrett–Munk $k_z^{-2}$, even though the GM spectrum is often attributed to weakly interacting waves. This discrepancy may result from our limited resolution, but it may also be due to the absence of vortical modes. When vortical modes are introduced into our wave-forced simulations, wave–vortical–wave interactions increase in importance and, when sufficient vortical energy is present, they account for most of the downscale transfer

https://doi.org/10.1017/S0022112005007111 Published online by Cambridge University Press

of wave energy. When waves and vortical modes are forced with equal amplitudes, the bumps disappear and the wave energy spectrum has a slope of approximately $-1.7$. This slope resembles the GM value of $-2$ as well as $-5/3$; more resolution is required to distinguish between these two possibilities. In any case, these results indicate that the presence of vortical motion can strongly affect the wave spectrum in the weakly nonlinear regime, and must be included in any explanation of the GM spectrum. The wave–vortical–wave interaction may also play an important role in the development of the atmospheric saturation spectrum, dissipating unsaturated waves as they propagate upward. The importance of this effect should be further investigated.

In our simulations, the slope of the energy spectrum is unaffected by changes in Reynolds number as long as the overturning scale is at least three times larger than the dissipation scale. Failure to satisfy this condition leads to a steepening of the spectrum and, in one case, a spurious $k_z^{-3}$. Care must be taken in interpreting the energy spectrum in such cases. In the ocean, $l_c \approx 10$ m. Vertical grid spacings in high-resolution ocean models are generally larger than $l_c$ below the mixed layer, and so this scale is not resolved (e.g. Smith *et al.* 2000). In the atmosphere, however, $l_c \approx 1$ km. High-resolution atmospheric models employ up to 100 grid points in the vertical, which yields grid spacings of hundreds of metres away from the boundary (e.g. Ohfuchi *et al.* 2004). Atmospheric models are therefore just beginning to resolve scales smaller than $l_b$. With such resolutions comes the potential to reproduce the observed vertical wavenumber energy spectrum, a possibility which should be explored.

The authors would like to thank G. Holloway, M.-P. Lelong and J. J. Riley for their helpful comments. Support from the Natural Sciences and Engineering Research Council of Canada and the Meteorological Service of Canada is also gratefully acknowledged, as are the computer resources generously provided by the Consortium Laval–UQAM–McGill et l'Est du Québec.

## REFERENCES

Alisse, J.-R. & Sidi, C. 2000 Experimental probability density functions of small-scale fluctuations in the stably stratified atmosphere. *J. Fluid Mech.* **402**, 137–162.

Allen, S. J. & Vincent, R. A. 1995 Gravity wave activity in the lower atmosphere: Seasonal and latitudinal variations. *J. Geophys. Res.* **100**, 1327–1350.

Asselin, R. 1972 Frequency filter for time integrations. *Mon. Wea. Rev.* **100**, 487–490.

Babin, A., Mahalov, A., Nicolaenko, B. & Zhou, Y. 1997 On the asymptotic regimes and the strongly stratified limit of rotating Boussinesq equations. *Theor. Comput. Fluid Dyn.* **9**, 223–251.

Bartello, P. 1995 Geostrophic adjustment and inverse cascades in rotating stratified turbulence. *J. Atmos. Sci.* **52**, 4410–4428.

Bartello, P., Métais, O. & Lesieur, M. 1996 Geostrophic versus wave eddy viscosities in atmospheric models. *J. Atmos. Sci.* **53**, 564–571.

Bartello, P. & Warn, T. 1996 Self-similarity of decaying two-dimensional turbulence. *J. Fluid Mech.* **326**, 357–372.

Benielli, D. & Sommeria, J. 1996 Excitation of internal waves and stratified turbulence by parametric instability. *Dyn. Atmos. Oceans* **23**, 335–343.

Billant, P. & Chomaz, J.-M. 2001 Self-similarity of strongly stratified inviscid flows. *Phys. Fluids* **13**, 1645–1651.

Bouruet-Aubertot, P., Sommeria, J. & Staquet, C. 1996 Stratified turbulence produced by internal wave breaking: Two-dimensional numerical experiments. *Dyn. Atmos. Oceans* **23**, 357–369.

Carnevale, G. F., Briscolini, M. & Orlandi, P. 2001 Buoyancy- to inertial-range transition in forced stratified turbulence. *J. Fluid Mech.* **427**, 205–239.

https://doi.org/10.1017/S0022112005007111 Published online by Cambridge University Press

Cho, J. Y. N., Newell, R. E. & Barrick, J. D. 1999 Horizontal wavenumber spectra of winds, temperature, and trace gases during the Pacific exploratory missions: 2. Gravity waves, quasi-two-dimensional turbulence, and vortical modes. *J. Geophys. Res.* **104**, 16297–16308.

Dewan, E. M. & Good, R. E. 1986 Saturation and the "universal" spectrum for vertical profiles of horizontal scalar winds in the atmosphere. *J. Geophys. Res.* **91**, 2742–2748.

Embid, P. F. & Majda, A. J. 1998 Low Froude number limiting dynamics for stably stratified flow with small or finite Rossby numbers. *Geophys. Astrophys. Fluid Dyn.* **87**, 1–50.

Gargett, A. E., Hendricks, P. J., Sanford, T. B., Osborn, T. R. & Williams III, A. J. 1981 A composite spectrum of vertical shear in the upper ocean. *J. Phys. Oceanogr.* **11**, 1258–1271.

Gargett, A. E., Osborn, T. R. & Nasmyth, P. W. 1984 Local isotropy and the decay of turbulence in a stratified fluid. *J. Fluid Mech.* **144**, 231–280.

Godeferd, F. S. & Cambon, C. 1994 Detailed investigation of energy transfers in homogeneous stratified turbulence. *Phys. Fluids* **6**, 2084–2100.

Hines, C. O. 1991 The saturation of gravity waves in the middle atmosphere. Part I: Critique of linear-instability theory. *J. Atmos. Sci.* **48**, 1348–1359.

Hines, C. O. 1996 Nonlinearity of gravity wave saturated spectra in the middle atmosphere. *Geophys. Res. Lett.* **23**, 3309–3312.

Holloway, G. 1982 On interaction time scales of oceanic internal waves. *J. Phys. Oceanogr.* **12**, 293–296.

Holloway, G. 1983 A conjecture relating oceanic internal waves and small-scale processes. *Atmos. Ocean* **21**, 107–122.

Itsweire, E. C., Helland, K. N. & Van Atta, C. W. 1986 The evolution of grid-generated turbulence in a stably stratified fluid. *J. Fluid Mech.* **162**, 299–338.

Laval, J.-P., McWilliams, J. C. & Dubrulle, B. 2003 Forced stratified turbulence: Successive transitions with Reynolds number. *Phys. Rev.* E **68**, 036308.

Lelong, M.-P. & Riley, J. J. 1991 Internal wave-vortical mode interactions in strongly stratified flows. *J. Fluid Mech.* **232**, 1–19.

Lumley, J. L. 1964 The spectrum of nearly inertial turbulence in a stably stratified fluid. *J. Atmos. Sci.* **21**, 99–102.

McComas, C. H. & Bretherton, F. P. 1977 Resonant interactions of oceanic internal waves. *J. Geophys. Res.* **82**, 1397–1412.

McComas, C. H. & Müller, P. 1981 Time scales of resonant interactions among oceanic internal waves. *J. Phys. Oceanogr.* **11**, 139–147.

Métais, O. & Lesieur, M. 1992 Spectral large-eddy simulation of isotropic and stably stratified turbulence. *J. Fluid Mech.* **239**, 157–194.

Müller, P., Holloway, G., Henyey, F. & Pomphrey, N. 1986 Nonlinear interactions among internal gravity waves. *Rev. Geophys.* **24**, 493–536.

Munk, W. 1981 Internal waves and small-scale processes. In *Evolution of Physical Oceanography* (ed. B. A. Warren & C. Wunsch), pp. 264–291. MIT Press.

Nastrom, G. D., VanZandt, T. E. & Warnock, J. M. 1997 Vertical wavenumber spectra of wind and temperature from high-resolution balloon soundings over Illinois. *J. Geophys. Res.* **102**, 6685–6701.

Ohfuchi, W., Nakamura, H., Yoshioka, M. K., Enomoto, T., Takaya, K., Peng, X., Yamane, S., Nishimura, T., Kurihara, Y. & Ninomiya, K. 2004 10-km mesh meso-scale resolving simulations of the global atmosphere on the earth simulator – preliminary outcomes of AFES (AGCM for the Earth Simulator). *J. Earth Simulator* **1**, 8–34.

Orlanski, I. & Cerasoli, C. P. 1981 Energy transfer among internal gravity modes: Weak and strong interactions. *J. Geophys. Res.* **86**, 4103–4124.

Polzin, K. L., Kunze, E., Toole, J. M. & Schmitt, R. W. 2003 The partition of finescale energy into internal waves and subinertial motions. *J. Phys. Oceanogr.* **33**, 234–248.

Riley, J. J. & Lelong, M.-P. 2000 Fluid motions in the presence of strong stable stratification. *Annu. Rev. Fluid Mech.* **32**, 613–657.

Smith, L. M. & Waleffe, F. 2002 Generation of slow large scales in forced rotating stratified turbulence. *J. Fluid Mech.* **451**, 145–168.

Smith, R. D., Maltrud, M. E., Bryan, F. O. & Hecht, M. W. 2000 Numerical simulations of the North Atlantic Ocean at 1/10°. *J. Phys. Oceanogr.* **30**, 1532–1561.

https://doi.org/10.1017/S0022112005007111 Published online by Cambridge University Press

Smith, S. A., Fritts, D. C. & VanZandt, T. E. 1987 Evidence for a saturated spectrum of atmospheric gravity waves. *J. Atmos. Sci.* **44**, 1404–1410.

Staquet, C. & Sommeria, J. 2002 Internal gravity waves: From instabilities to turbulence. *Annu. Rev. Fluid Mech.* **34**, 559–593.

Thorpe, S. A. 1977 Turbulence and mixing in a Scottish Loch. *Phil. Trans. R. Soc. Lond.* A **286**, 125–181.

Tsuda, T., Inoue, T., Fritts, D. C., VanZandt, T. E., Kato, S., Sato, T. & Fukao, S. 1989 MST radar observations of a saturated gravity wave spectrum. *J. Atmos. Sci.* **46**, 2440–2447.

Waite, M. L. & Bartello, P. 2004 Stratified turbulence dominated by vortical motion. *J. Fluid Mech.* **517**, 281–308.

Yoshida, K., Ishihara, T. & Kaneda, Y. 2002 LES of stably stratified turbulence. In *Statistical Theories and Computational Approaches to Turbulence* (ed. Y. Kaneda & T. Gotoh), pp. 219–228. Springer.

https://doi.org/10.1017/S0022112005007111 Published online by Cambridge University Press